PHYSICAL REVIEW E **108**, 054219 (2023)

Ergodicity of complex dynamics and quantum tunneling in nonintegrable systems

Ryonosuke Koda,[1] Yasutaka Hanada,[2] and Akira Shudo[1]
[1]*Department of Physics, Tokyo Metropolitan University, Tokyo 192-0397, Japan*
[2]*Department of Information Science, Faculty of Arts and Sciences, Showa University, Yamanashi 403-0005, Japan*

(Received 8 August 2023; accepted 11 October 2023; published 21 November 2023)

The instanton approximation is a widely used approach to construct the semiclassical theory of tunneling. The instanton path bridges the regions that are not connected by classical dynamics, but the connection can be achieved only if the two regions have the same energy. This is a major obstacle when applying the instanton method to nonintegrable systems. Here we show that the ergodicity of complex orbits in the Julia set ensures the connection between arbitrary regions and thus provides an alternative to the instanton path in the nonintegrable system. This fact is verified using the ultra-near integrable system in which none of the visible structures inherent in nonintegrability exist in the classical phase space, yet nonmonotonic tunneling tails emerge in the corresponding wave functions. The simplicity of the complex phase space allows us to explore the origin of the nontrivial tunneling tails in terms of semiclassical analysis in the time domain. In particular, it is shown that not only the imaginary part but also the real part of the classical action plays a role in creating the characteristic step structure of the tunneling tail that appears as a result of the quantum resonance.

DOI: 10.1103/PhysRevE.108.054219

I. INTRODUCTION

The mechanism of quantum tunneling in nonintegrable systems is not fully understood despite the fact that nearly 40 years have passed since the concept *dynamical tunneling* was introduced [1–3]. Although several scenarios have been proposed [4–12], including the theory based on fully complex semiclassical analysis, we are still far from a complete understanding of the essential difference between the nature of tunneling in completely integrable and nonintegrable systems.

Dynamical tunneling is a quantum process in terms of which the wave packet penetrates regular regions covered by Kolmogorov-Arnold-Moser (KAM) tori (or curves) in phase space. It is a transport consisting of penetration through the regular region and propagation in the chaotic sea. The whole process is a complicated mixture of classically forbidden and allowed processes. The term "tunneling coupling between regular and chaotic states" is often used, but it would be actually difficult to give a precise definition for it. One may introduce tunneling couplings phenomenologically in a certain matrix representation of Hamiltonians [4,5], but it is by no means obvious which basis functions to choose and how to explicitly evaluate the strength of tunneling couplings from the first principle.

It is well known that the eigenstates with an identical energy but different parities are quasidegenerate and give rise to exponentially small energy splittings [13–15]. Although the tunneling splitting is created as a result of the quantum effect, it is possible to evaluate the splitting width in terms of the classical orbit if one is allowed to use the complex plane. The so-called *instanton* is a complex classical path connecting the two separated wells, and the associated classical action is known to provide the splitting width [13–15]. The theory using complex paths was first developed in field theory [15–17] and in chemical reactions [18,19]. In this sense the complex path method is not particularly new, but rather a common practice. It is important to note that the instanton method can be applied only to integrable systems, as will be discussed in more detail below.

On the other hand, in nonintegrable systems we encounter many difficulties, not only because of the absence of the instanton path, which makes the alternative complex dynamics completely different, but also because of the lack of semiclassical formulations in the energy domain. The latter problem prevents us from using the complex path method to compute quantities related to the eigenvalues of the system. Although tunneling splittings also appear in dynamical tunneling problems [4–7,11,12], we do not have any fully explicit semiclassical expressions for the width of tunneling splittings. In strongly chaotic systems, the Gutzwiller trace formula connects the eigenvalue sequence of the quantum systems to the set of the periodic orbits in the corresponding classical systems [20,21], but in mixed systems where regular and chaotic regions coexist in a single phase space, such a formula does not exist even in the semiclassical analysis in the real domain. The most that can be done is to develop the analysis in the time domain.

What is more serious, but unavoidable, is that it is not easy to identify a set of complex paths that control dynamical tunneling in nonintegrable situations, even if one performs the semiclassical calculation in the time domain [9,10,22]. Here we will not go into detail about the Stokes phenomenon, i.e., the birth and death of the saddle points or WKB solutions, which occurs in the asymptotic analysis in general [23–26]. It is inevitable to deal with the Stokes phenomenon when applying the complex semiclassical method, but here we mention only that the aspect of the Stokes phenomenon becomes much more involved and requires more newly developed ideas to tackle than one-dimensional situations [27–29].

We focus here on the problem of how to sort out the most dominant set of complex paths from potential candidates whose number grows exponentially with time or, in some classes of systems, infinitely many even within a finite time. This has been partially solved based on recent results in the theory of complex dynamical systems [30–34]. The results show that the orbits contained in the Julia set control the dynamical tunneling, and the rest of the orbits have no chance to contribute [35–37]. This finding would be suggestive for our central question, i.e., the essential difference of tunneling between integrable and nonintegrable systems, since it is known that chaotic behavior is observed only in the Julia set [30–34], which in turn implies that tunneling transport is driven by chaotic orbits in the complex plane.

Further analysis has allowed a more detailed identification of the complex orbits that are most dominant in the Julia set [38]. This can be achieved by using a theorem, which asserts that stable (or unstable) manifolds for any unstable periodic point are dense in the forward (resp. backward) Julia set [30–33]. The complex orbits that produce the tunneling transport are guided by stable manifolds associated with unstable periodic orbits on the real chaotic sea [35–37,39]. This mechanism is called the *complexified stable manifold mechanism*. It was found in [38] that the orbits tending to the sticky zone around the KAM region provide the most dominant contribution in the semiclassical sum. This is consistent with earlier results [8,40], which emphasized the importance of the so-called beach state.

We should point out that there is a drawback to the time-domain semiclassical analysis. As mentioned above, dynamical tunneling is a process that proceeds in a mixture of classically forbidden and allowed processes. Time-domain semiclassical calculations can provide only transition probabilities associated with this entire process. In other words, one cannot clearly separate the contribution from the pure tunneling process in the KAM regime from the process involving chaotic transport. The complexified stable manifold mechanism assumes the periodic orbits in the real chaotic sea, and thus the second half of the process is inevitably influenced by the transport in the real plane.

It may be tempting to study the system with sharply divided phase space [41,42] in order to separate the transport within the regular region from the propagation in the chaotic sea. However, the diffraction effect now enters and dominates the transition process there [43]. Diffraction is also a kind of a purely wave effect like the tunneling effect, but its nature or $\hbar$ dependence is different.

The main objective of this work is to elucidate the mechanism of tunneling transport within the KAM region using the complex path approach. To eliminate the influence of chaotic regions, we will prepare a system sufficiently close to a certain integrable limit. By doing so, we suppress the complexified stable manifold mechanism as much as possible. Nevertheless, we can observe that dynamical tunneling occurs, and the complex paths carry the tunneling amplitude as shown in this work.

To realize the situation where the influence of chaos is minimal, we consider an *ultra-near integrable system*, which was recently introduced in Ref. [44]. We say that the system is ultra-near integrable if the system is sufficiently close to a certain integrable limit such that none of the classical invariant structures inherent in nonintegrability are visible in the classical phase space, compared to the scale of the Planck cell. In other words, the ultra-near integrable system is a kind of relative concept and can be defined only through the reference quantum system. Obviously, by definition, all the scenarios proposed so far to describe dynamical tunneling in nonintegrable systems, such as chaos-assisted tunneling (CAT) [4,5,45] or resonance-assisted tunneling (RAT) [6,7], could not be applied, since they all assume chaotic regions or nonlinear resonances in the size of the Planck cell.

As discovered in Ref. [44], tunneling tails of eigenfunctions of ultra-near integrable systems exhibit unexpected profiles under a certain condition. Arbitrary precision arithmetic calculations have revealed that the tunneling tails do not obey any law derived from existing theories developed so far, despite the fact that visible invariant structures associated with nonintegrability are absent in the corresponding phase space. The ultra-near integrable system would therefore provide us with an opportunity to delve deeper into the problem of tunneling in nonintegrable systems. In particular, one could answer the question why dynamical tunneling proceeds even without instanton paths, or more generally, without using any type of integrable approximation. We can expect that this would lead to a solution to our ultimate question, the essential difference between the nature of tunneling in completely integrable and nonintegrable systems.

The outline of this paper is as follows: In Sec. II we show the results of fully quantum mechanical calculations for our ultra-near integrable system. The calculation using arbitrary-precision arithmetic shows that the nontrivial step structure appears in the tunneling tail. This was first found in Ref. [44] for the eigenstates, but here we show that it also appears in the time evolution of the wave packet. To make the present paper self-contained, we will include the results for the eigenstates and point out the mechanism that produces the step structure.

Section III provides the formulation of the time-domain semiclassical analysis, which simply follows the standard recipe.

In Sec. IV we discuss the ergodicity of the dynamics in the complex plane. Our argument is based on rigorous mathematical results on the polynomial maps in $\mathbb{C}^2$, where mixing and thus ergodicity hold in the so-called potential-theoretic Julia set J^*. However, since the set J^* is not directly accessible by numerical computation, we need to verify that ergodicity also holds in the Julia set J, which is an invariant set naturally introduced in the complex plane. We give numerical evidence that the dynamics of the Julia set J is ergodic even in the case where the map contains a transcendental function.

Section V is devoted to showing how to find the complex orbits with the minimal imaginary action. In nonintegrable systems, the number of semiclassically contributing complex saddle solutions grows exponentially with time, although the underlying real classical phase space is predominantly covered by KAM curves. The task of finding the most dominant complex orbit(s) is therefore important but highly nontrivial. The advantage of using the ultra-near integrable system is that not only in the real plane, but also in the complex plane, the orbits are almost governed by rotational motions associated with KAM curves. We classify the complex orbits according to the type of rotational domains in the complex plane. This leads to a recipe for finding the complex orbit(s) with the minimal imaginary actions. It is found that the step height found in the tunneling tail is consistent with the imaginary action found in this way. We show that the nontrivial stretched exponential dependence of the step height on the Planck constant can be reproduced by the semiclassical calculation.

Section VI discusses the role of the real action in the semiclassical argument. As shown in Ref. [44], the step structure arises as a result of quantum resonance, and the position of the step moves with the change of the Planck constant. This implies that the interference mechanism works to create the resonance. From this perspective, we investigate the role of the real action and show a possible semiclassical mechanism leading to the quantum resonance observed in pure quantum calculations.

Section VII gives the conclusion and outlook of the paper. In particular, we discuss the difference between the nature of tunneling in completely integrable and nonintegrable systems in view of the nature of the complex dynamics describing tunneling. We also emphasize that the semiclassical mechanism found here works not only in ultra-near integrable settings, but also in more generic systems where both regular and chaotic regions are visible in the corresponding phase space. This would lead to a reconsideration of existing theories of quantum tunneling in nonintegrable systems.

II. TUNNELING TAILS FOR ULTRA-NEAR INTEGRABLE SYSTEMS

A. Classical and quantum map

As a model of nonintegrable systems, we consider the periodically kicked rotor,

$$H(p, q, t) = T(p) + \tau V(q) \sum_n \delta(t - n\tau). \tag{1}$$

Here the parameter τ controls the role of the period of perturbation, and at the same time it gives the kicking strength. The functions $T(p)$ and $V(q)$ denote kinetic and potential functions, respectively. The angular frequency for the periodic driving is given by $\Omega = 2\pi/\tau$.

As usual, the classical time evolution is expressed as

$$f : \begin{pmatrix} q \\ p \end{pmatrix} \mapsto \begin{pmatrix} q + \tau T'(p) \\ p - \tau V'[q + \tau T'(p)] \end{pmatrix}. \tag{2}$$

The prime stands for the derivative with respect to the argument. In the limit of $\tau \to 0$, the classical map f tends to a continuous time flow system generated by the one-dimensional Hamiltonian $\mathcal{H}(p, q) = T(p) + V(q)$.

Time evolution of the corresponding quantum system is described by the unitary operator,

$$\hat{U} = \exp\left(-\frac{i\tau}{\hbar} V(\hat{q})\right) \exp\left(-\frac{i\tau}{\hbar} T(\hat{p})\right), \tag{3}$$

which will be referred to as the quantum map hereafter.

The eigenvalue equation for the quantum map is given by

$$\hat{U}|\Psi_k\rangle = u_k|\Psi_k\rangle \quad \text{with} \quad u_k = \exp\left(-\frac{i\tau}{\hbar} E_k\right), \tag{4}$$

where E_k and $|\Psi_k\rangle$ are quasi-eigenenergy and the associated quasi-eigenstate, respectively. The eigenvalues are distributed on the unit circle, which reflects the time periodicity of the Hamiltonian (1). Here we assign the quantum number of quasi-eigenstates in the ascending order of the eigenvalues for the one-dimensional continuous Hamiltonian $\mathcal{H}(q, p)$.

B. Classical phase space for ultra-near integrable systems

Below we consider the case with the kinetic term $T(p) = p^2/2$ and take the potential function

$$V(q) = \frac{1}{2}q^2 - 2\varepsilon \cos\left(\frac{q}{\lambda}\right), \tag{5}$$

where λ and ε are the parameters specifying the length of modulation and the perturbation strength to the harmonic term, respectively. Recall that a similar potential function was used in Ref. [46], but the error function was present there.

For $\tau \ll 1$, the system becomes close to the one-dimensional continuous Hamiltonian $\mathcal{H}(p, q)$, thus the phase space is almost covered by KAM curves, as displayed in Fig. 1. When the parameter ε is small, the KAM circles are slightly deformed due to the presence of the modulation term in the potential $V(q)$. The reason for calling such a situation ultra-near integrable is that the structures, such as Poincaré-Birkhoff chains or stochastic layers around the separatrix, are invisible compared to the size of the Planck cell. In other words, if the size of the Planck constant is small enough to resolve the structures of nonintegrability origin, we do not refer it to ultra-near integrable systems.

C. Tunneling tails of eigenfunctions

A natural expectation for the profile of the eigenfunctions would be that they exhibit a simple monotonic decay, as the $\tau \to 0$. However, as seen in Fig. 2(a), the ground state $|\langle q|\Psi_0\rangle|^2$ does not yield a monotonically decaying profile, but the staircase structure appears in the tunneling tail when ε is set large. Here numerical calculations have been performed using the Advanpix Multiprecision Computing Toolbox for MATLAB [47], which allows one to raise the precision arbitrarily as far as the computational time is permitted [44].

For comparison, we plot the eigenfunctions for the one-dimensional continuous Hamiltonian, which is obtained by solving the eigenvalue equation,

$$\hat{H}^{(M)}_{q\mathrm{BCH}}|\Phi^{(M)}_k\rangle = E^{(M)}_k|\Phi^{(M)}_k\rangle, \tag{6}$$

where $E^{(M)}_n$ and $|\Phi^{(M)}_n\rangle$ denote eigenvalues and the associated eigenfunctions for the Hamiltonian,

$$\hat{H}^{(M)}_{q\mathrm{BCH}} = \sum_{j=1}^{M} \left(\frac{\tau}{\mathrm{i}\hbar}\right)^{j-1} \hat{H}_j. \tag{7}$$

Here $\hat{H}^{(M)}_{q\mathrm{BCH}}$ is obtained by truncating the Baker-Campbell-Hausdorff (BCH) Hamiltonian defined through the relation

$$\exp\left(-\frac{\mathrm{i}\tau}{\hbar} V(\hat{q})\right) \exp\left(-\frac{\mathrm{i}\tau}{\hbar} T(\hat{p})\right) = \exp\left(-\frac{\mathrm{i}\tau}{\hbar} \hat{H}_{\mathrm{BCH}}\right), \tag{8}$$

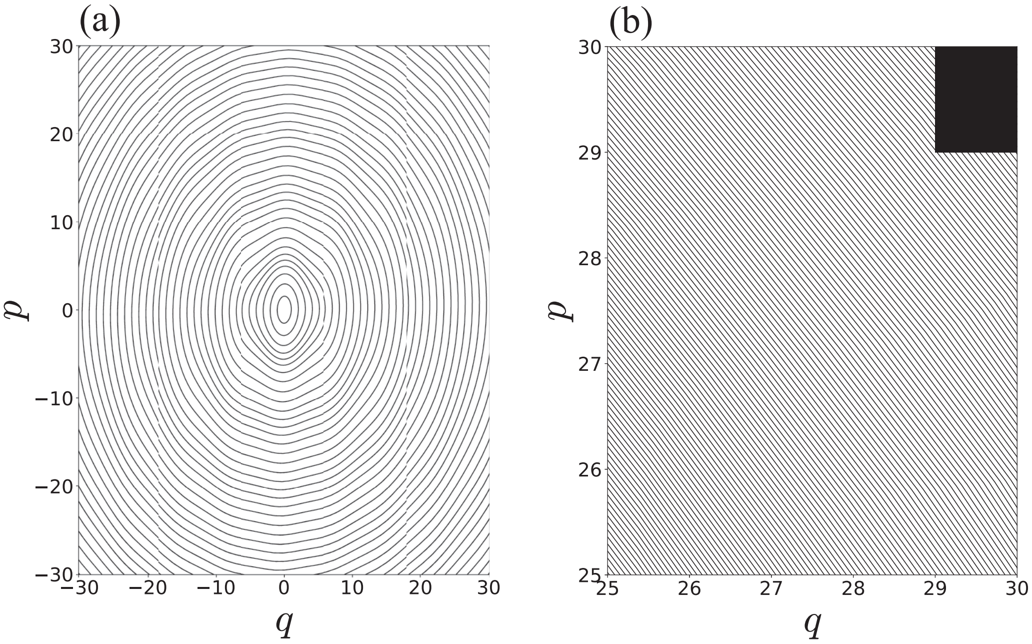

FIG. 1. (a) Phase space profile of the classical map (2). The parameters of the potential function (5) are set to $\varepsilon = 1.0$, $\tau = 0.05$, and $\lambda = 1.2$. The plot (b) is a magnification of the plot (a). The black box put in the upper-right corner represents the Planck cell with $\hbar = 1$.

where

$$\hat{H}_{\mathrm{BCH}} = \hat{H}_1 + \left(\frac{\tau}{\mathrm{i}\hbar}\right)\hat{H}_2 + \left(\frac{\tau}{\mathrm{i}\hbar}\right)^2\hat{H}_3 + \cdots . \tag{9}$$

Explicit expressions for $\hat{H}_n$ ($n \in \mathbb{N}$) can be derived from the BCH formula.

As demonstrated in Ref. [44], the KAM curves for the classical map shown in Fig. 1 are perfectly approximated by the classical analog of the truncated quantum BCH Hamiltonian. Therefore, $\hat{H}^{(M)}_{q\mathrm{BCH}}$ can be a good candidate for the instanton approximation or direct tunneling [42,48,49]. As verified in Ref. [44], the profile of $|\langle q|\Phi^{(M)}_0\rangle|^2$ does not change even with increasing truncation order M, implying that the original system is already sufficiently close to the integrable limit $\mathcal{H}(q,p)$. The reason why the step structure appears in Fig. 2(a) and not in Fig. 2(b) will be discussed in Sec. V F.

We cannot immediately conclude that the observed step structure originates from the nonintegrability of the system only because the eigenfunction of the quantum map does not have a monotonic tunneling tail but creates the step structure. To show this, we consider the one-dimensional Hamiltonian in a normal form, which is similar to the normal form studied in [50,51]:

$$H(q,p) = H_0(q,p) + \varepsilon H_1(q,p) \tag{10}$$

with

$$H_0(q,p) = \tfrac{1}{2}(q^2+p^2) + a(q^2+p^2)^2, \tag{11a}$$

$$H_1(q,p) = p^4 - 6p^2q^2 + q^4. \tag{11b}$$

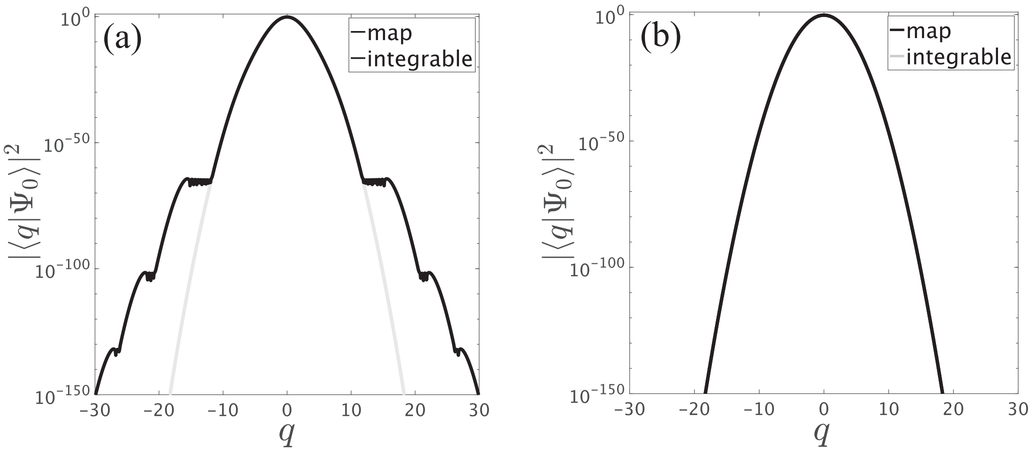

FIG. 2. The black curve shows the ground-state eigenfunction for the quantum map (4), and the gray one shows that for the truncated quantum BCH Hamiltonian $\hat{H}^{(M)}_{q\mathrm{BCH}}$ with $M = 3$. The parameters in the potential function (5) are set to (a) $\lambda = 1.2$ and (b) $\lambda = 3.0$, respectively. The remaining parameters are set to $\tau = 0.05$, $\varepsilon = 1.0$, and $\hbar = 1$.

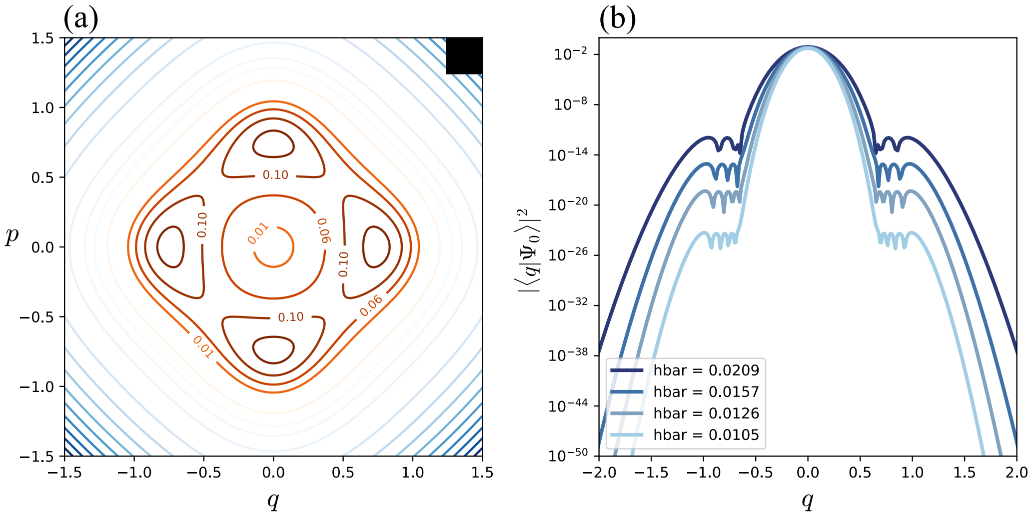

FIG. 3. (a) Classical phase space profile for the Hamiltonian (10). (b) The ground-state quantum eigenfunction with different values of the Planck constant. The corresponding eigenvalue is $E_0 = 6.24 \times 10^{-3}$. The black box at the right upper corner in the plot (a) represents the Planck cell for the case of $\hbar = 0.0105$. The parameters in Eqs. (10) and (11a) are set to $a = -0.55$ and $\epsilon = 0.1$.

In Fig. 3 we give the classical phase space profile and the ground-state eigenfunction for the corresponding quantum Hamiltonian. Clearly, the step structure appears in the tunneling tail, which is exactly where the island-like equi-energy contours appear in the corresponding classical phase space. Therefore, the nonmonotonic tunneling tail does not necessarily imply that the system is nonintegrable. It is important to note that, as shown in Fig. 3(b), the position of the step does not move in the q direction with the change of the Planck constant $\hbar$. As pointed out below, this is in sharp contrast to the ultra-near integrable situation.

Note that the island-like equi-energy contours are not nonlinear resonances because the system is one-dimensional and thus resonance cannot happen there. The staircase in this case consists of only one step, but in principle one could construct the one-dimensional Hamiltonian whose eigenfunctions mimic the staircase with multiple steps. However, this does not help to explain the observed phenomenon.

D. Planck constant dependence of the step structure

It would not be reasonable to hypothesize that the RAT mechanism works in the ultra-near integrable situation. First, as seen in Fig. 1, the nonlinear resonances, if any, are too small compared to the size of the Planck cell. The RAT mechanism is supposed to start only after the Planck cell resolves nonlinear resonances [42]. Before the RAT regime, the direct tunneling mechanism dominates, and a simple exponential decay without any specific structures is expected in the tunneling rate γ [42] (or the tunneling splitting ΔE) vs $1/\hbar$ plot [52]. The existence of the direct tunneling regime could be intuitively understood by the fact that the Planck cell smears out the underlying classical structures. As the effective Planck constant becomes smaller, nonlinear resonances become visible. As a result, the transition from direct to RAT-driven tunneling is expected to take place. This is the scenario assumed in the RAT theory.

On the other hand, apart from the standard RAT scenario, one might think that extremely small nonlinear resonances could affect extremely small tunneling tails. It must be true that any invariant structure, no matter how small, will in principle leave some form of fingerprints on the corresponding quantum wave function. However, if the size of such nonlinear resonances is too small compared to the width of the step observed here, they cannot be the support of the step structure. Too thin nonlinear resonances cannot cover widespread plateaus in the q direction.

More decisive evidence to exclude the possible role of nonlinear resonances is the $\hbar$ dependence of the step structure presented in Fig. 4. If the step structure were linked to some classical invariant objects, the steps should have kept the same position even if the Planck constant was changed. Recall that this is exactly realized in the integrable model examined above. The RAT assumes that the coupling is mediated by classical resonances, so that the resulting structure in the tunneling tail should be attached to the associated nonlinear resonances. This means that the step should not move with the change of the Planck constant, just like the situation shown in Fig. 3(b). It would not be possible to explain the $\hbar$-dependent behavior within the RAT scenario. On the contrary, none of the scenarios based on certain classical invariant structures can explain the $\hbar$-dependent staircase structure [4–7,42,45,53–57].

Observation of the wave function amplitude at a certain fixed position reveals a nontrivial $\hbar$ dependence. As illustrated in the inset of Fig. 4, the wave function amplitude for the truncated quantum BCH Hamiltonian $\hat{H}^{(M)}_{q\mathrm{BCH}}$ exhibits a simple exponential decay, as expected. On the other hand, the amplitude of the eigenfunction for the quantum map shows an exponential decay in a large $\hbar$ regime, but it switches to a stretched exponential-type decay. The slope returns to 1 for smaller $\hbar$. Notice that stretched exponential regions appear when the observation points hit a plateau region of the wave function. We recall that similar behavior has also been found in tunneling splitting vs $1/\hbar$ plot [52], where nonexponential regions appear due to the quantum resonance between the

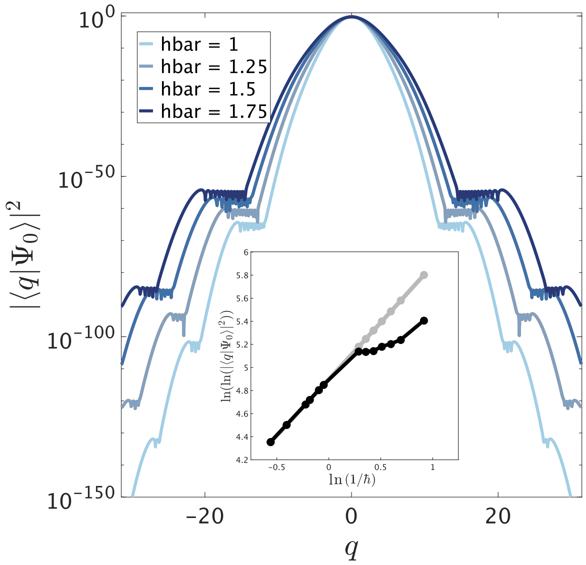

FIG. 4. Ground-state eigenfunction for the quantum map (4) with different values of the Planck constant. (Inset) Magnitude of the ground-state eigenfunction at a fixed position ($q = 11$) plotted as a function of $1/\hbar$. Black and gray curves show the ground-state eigenfunction for the quantum map (4) and for the truncated quantum BCH Hamiltonian $\hat{H}^{(M)}_{q\mathrm{BCH}}$ with $M = 3$, respectively. In both panels, the other parameters are set to $\tau = 0.05$, $\varepsilon = 1.0$, and $\lambda = 1.2$.

librational and rotational states, i.e., the *coupling across the separatrix* in the phase space.

E. Quantum resonance

As clarified in Ref. [44], both the step structure and its $\hbar$ dependence are explained as manifestations of the *quantum resonance*. Here we show that the excited states satisfying the quantum resonance condition produce the step structure in the tunneling tail. Figure 5(a) plots the ground state under the the quantum BCH basis $|\Phi^{(M)}_k\rangle$ in logarithmic scale. We can see that the ground state of the quantum map is well approximated by that of the BCH basis, which is manifested by a sharp drop of the curve near the ground-state energy. After this initial drop, the curves decay overall exponentially, except for small peaks indicated by the arrows in the plot.

The eigenvalues corresponding to the peaks can be read off from Fig. 5(a). That is, the component $\langle\Phi^{(M)}_k|\Psi_0\rangle$ takes a large value when the resonance condition

$$E^{(M)}_k = E^{(M)}_0 + mE_{\mathrm{ex}}, \quad m \in \mathbb{N} \tag{12}$$

is satisfied. Here note that the energy associated with the periodic kick is given by $E_{\mathrm{ex}} := 2\pi\hbar/\tau$. This condition (12) can also be derived from the perturbation analysis [44]. That is, taking the BCH Hamiltonian $H^{(M)}_{c\mathrm{BCH}}$ as the unperturbed Hamiltonian, the time-dependent perturbation calculation tells us that the resonance condition (12) is given by the condition that the denominator of the first-order perturbative term is zero.

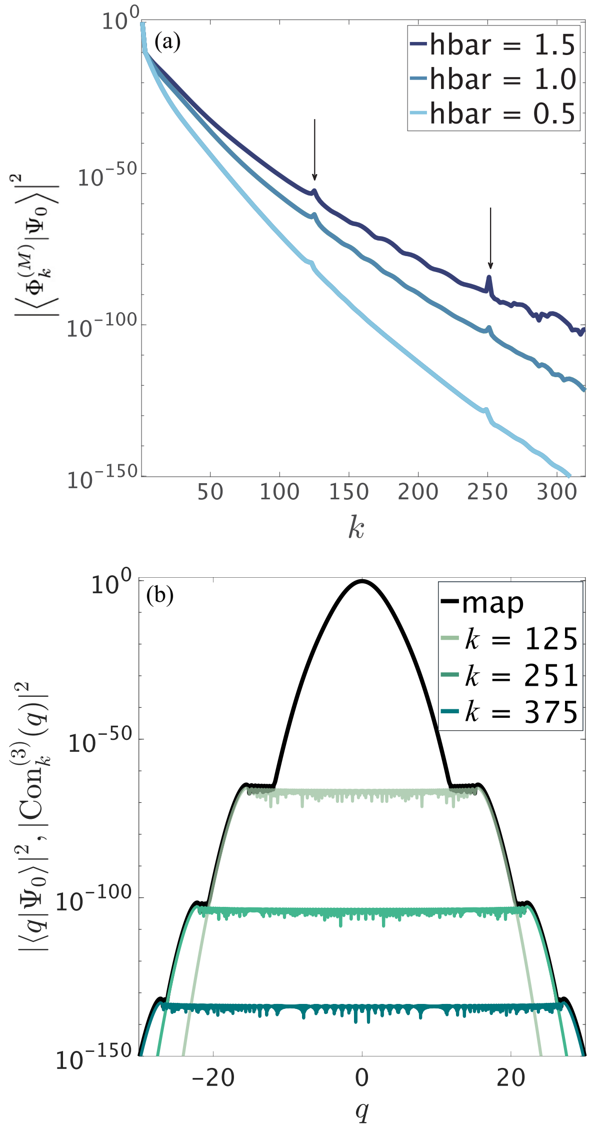

FIG. 5. (a) Ground-state eigenfunctions in the quantum BCH representation $|\Phi^{(M)}_k\rangle$ with $M = 3$ for different values of $\hbar$. (b) Ground-state eigenfunction in the q representation in the case $\hbar = 1$ (black). The states, $k = 125$, $k = 251$, and $k = 375$ in the sum (13), are superposed and shown in different green colors. These states are responsible for the small peaks indicated by the arrows in plot (a). The parameters are set to $\tau = 0.05$, $\varepsilon = 1.0$, and $\lambda = 1.2$.

We can directly confirm that the coupling with the states creating small peaks in the plot of $|\langle\Phi^{(M)}_k|\Psi_0\rangle|^2$ is responsible for the staircase found in the plot of $|\langle q|\Psi_0\rangle|^2$ (see Fig. 3). To this end, we expand the ground state as [52]

$$\langle q|\Psi_0\rangle = \sum_k \langle q|\Phi^{(M)}_k\rangle\langle\Phi^{(M)}_k|\Psi_0\rangle. \tag{13}$$

Instead of taking the sum over all states k, we include only the states responsible for generating the peaks observed in Fig. 5(a). As shown in Fig. 5(b), the resulting state reproduces the observed staircase in the eigenfunction.

The role of quantum resonance has also been emphasized in nearly integrable situations [52]. For the standard map in a nearly integrable regime, the component $|\langle\Phi^{(M)}_k|\Psi_0\rangle|^2$ exhibits a series of equally spaced peaks at the energies satisfying the same quantum resonance condition (12). As a result, the staircase structure appears in the tunneling splitting

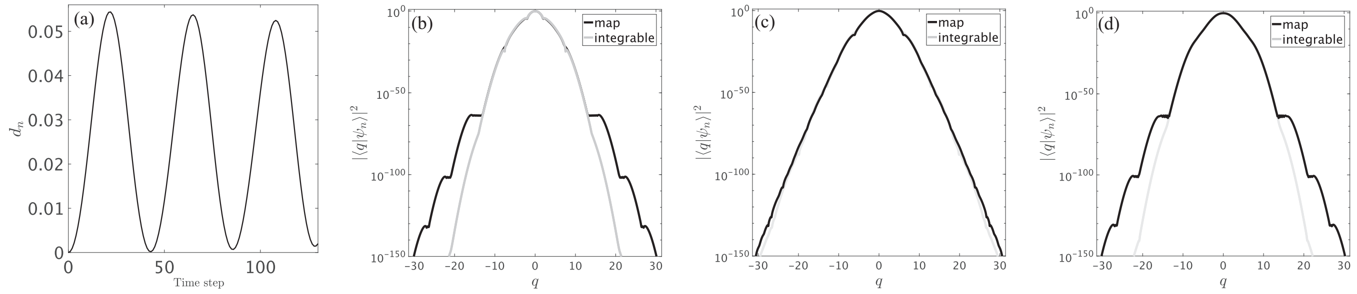

FIG. 6. (a) The variation of the difference d_n between the time evolution of the quantum map and that of the quantum BCH Hamiltonian with $M = 3$ [see Eq. (15)]. Snapshots of the time-evolved wave function at (b) $n = 63$, (c) $n = 94$, and (d) $n = 126$ in case of $\hbar = 1$. The parameters in the potential function (5) are set to $\tau = 0.05$, $\varepsilon = 1.0$, and $\lambda = 1.2$, respectively.

ΔE vs $1/\hbar$ plot. In contrast to the spikes associated with classical nonlinear resonances [52], the staircase in the ΔE vs $1/\hbar$ plot induces the *persistent enhancement* of tunneling splittings. Here the persistent enhancement is referred to as a phenomenon in which the anomalous enhancement of the splitting compared to the integrable limit is persistently maintained with the change of $1/\hbar$. The staircase structure observed in the splitting plot becomes less clear as the perturbation strength τ increases [52]. This is because the classical phase space becomes more complicated when the system is not sufficiently close to the integrable limit. In this respect, the ultra-near integrable system is a simpler or more ideal model than the system with a relatively large perturbation. For this reason, we can expect that the study of ultra-near integrable systems will advance our understanding of persistent enhancement.

F. Time evolution of wave packet and staircase structure

In the following sections we will seek a semiclassical understanding of the step structure observed above. However, as mentioned in Sec. I, there is no semiclassical formula that provides eigenfunctions of nonintegrable systems, and so the most we can do is to perform the semiclassical analysis in the time domain. We thus study the time-dependent problem, instead of observing the eigenfunctions.

Here we observe the time evolution of the coherent state,

$$\langle q|\psi_0\rangle = \left(\frac{1}{\pi\hbar}\right)^{\frac{1}{4}} \exp\left[-\frac{1}{2\hbar}(q - \langle q\rangle_\alpha)^2 + \frac{i}{\hbar}\langle p\rangle_\alpha (q - \langle q\rangle_\alpha)\right]. \tag{14}$$

The center of the wave packet is chosen as $(\langle q\rangle_\alpha, \langle p\rangle_\alpha) = (0, 0)$. Since the potential (5) is close to the harmonic potential when $\varepsilon \ll 1$, this initial packet is close to the ground state of the quantum map. As a result, we may expect that the initial wave packet is strongly coupled to the states satisfying the quantum resonance condition (12).

Figure 6(a) plots the difference between the time evolution of the quantum map and that of the BCH Hamiltonian with $M = 3$ as a function of the time step. The difference is measured using the norm defined by

$$d_n := \int_{-\infty}^{\infty} |\langle q|\hat{U}^n|\psi_0\rangle - \langle q|e^{-\frac{i}{\hbar}(\hat{H}^{(M)}_{q\mathrm{BCH}})n}|\psi_0\rangle|^2 dq. \tag{15}$$

As can be clearly seen, the wave function of the quantum map oscillates periodically in time, and the period can be estimated in terms of the oscillation period of the states satisfying the quantum resonance condition. Recall that the time evolution of the coherent state $|\psi_0\rangle$ is expressed using the definition $E_{\mathrm{ex}} = 2\pi\hbar/\tau$ as

$$\langle q|\hat{U}^n|\psi_0\rangle = \sum_k \exp\left(-\frac{2\pi \mathrm{i} E_k}{E_{\mathrm{ex}}} n\right)\langle q|\Psi_k\rangle\langle\Psi_k|\psi_0\rangle. \tag{16}$$

Considering the phase part depending on the time step n, we find that the period N during which the ground state $|\Psi_0\rangle$ returns to the initial phase is given by the condition $(E_0/E_{\mathrm{ex}})n = 1$, which leads to $N = E_{\mathrm{ex}}/E_0$. Since the coherent state (14) is close to the ground state $|\Psi_0\rangle$, we can expect that the projection $\langle\Psi_0|\psi_0\rangle$ to be maximum among others. As can indeed be verified in Fig. 6, the profile of the absolute value $|\langle q|\hat{U}^n|\psi_0\rangle|^2$ becomes close to that of the ground state at $n = kN/2$ $(k \in \mathbb{N})$.

The periodic revival allows us to study the origin of the step structure based on the time-domain semiclassical approach. The strategy adopted below is essentially the same as that used in the time-domain semiclassical analysis for the mixed phase space situation [9,10]. However, chaos in the real plane plays a significant role in the mixed phase space case, whereas the *rotational domains* in the complex plane control the observed feature of tunneling, as explained below.

III. TIME-DOMAIN SEMICLASSICAL PROPAGATOR

In the following, we develop the time-domain semiclassical analysis in the complex domain. We will use the standard formulation based on the Van Vleck–Gutzwiller propagator [20,58].

In the previous subsection we took the coherent state as the initial state of the time evolution and observed the time evolved wave function in the q representation. We therefore consider the propagator $\langle q|\hat{U}^n|E\rangle$ where n denotes the time step. The propagator is expressed in a discrete Feynman path integral form:

$$\langle q|\hat{U}^n|E\rangle = \int \cdots \int \prod_j dq_j \prod_j dp_j \exp\left(\frac{\mathrm{i}}{\hbar} S_n(q, E)\right). \tag{17}$$

As mentioned above, the coherent state $|\psi_0\rangle$ is close to the ground state $|\Psi_0\rangle$ of the quantum map, and the support of the state $|\Psi_0\rangle$ can be well expressed by the action variable E, since the system is ultra-near integrable. Thus, we denote the variable representing the initial coherent state $|\psi_0\rangle$ by the symbol E. The classical action is written as

$$S_n(q,E) = \sum_{j=1}^{n}\left[(q_j - q_{j-1})p_j - \frac{\tau}{2}p_j^2 - \tau V(q_{j-1})\right] + G(q_0,E), \tag{18}$$

where $G(q,E)$ is the generating function leading to the transformation from the original coordinate (q,p) to the action-angle variable (E,θ):

$$G(q,E) = \int^q p(q,E)\,dq. \tag{19}$$

The function $p(q,E)$ is obtained by solving the condition $E(q,p) = \text{const}$, where the constant specifies the position of the initial classical manifold.

As a simple choice, we take an ellipse as the initial condition. More specifically, the initial manifold is determined by fitting a rotated ellipse,

$$\Gamma : c_{11}q^2 + 2c_{12}qp + c_{22}p^2 = 1, \tag{20}$$

to the orbits numerically generated from an initial point on the manifold with $E_0^{(M)} = -1.24$. The lengths of the major and minor axes of the ellipse are expressed as $1/\sqrt{\lambda_1}$ and $1/\sqrt{\lambda_2}$, respectively, where λ_1 and λ_2 ($\lambda_1 < \lambda_2$) are the eigenvalues of the matrix c_{ij}. The rotating angle of the ellipse is given by $\alpha = \tan^{-1}(v_{12}/v_{11})$, where (v_{11}, v_{12}) is the eigenvector associated with λ_1. The generating function $G(q,E)$ is then written with the angle variable θ, which is conjugate to the action variable E, as

$$G(q,E) = \frac{1}{2\sqrt{\lambda_1\lambda_2}}\left(\theta + \frac{1}{2}\sin 2\theta\cos 2\alpha\right) - \frac{1}{8}\left(\frac{1}{\lambda_1} + \frac{1}{\lambda_2}\right)\cos 2\theta\sin 2\alpha. \tag{21}$$

To perform the semiclassical analysis in the complex domain, the initial manifold specified by the action variable E has to be complexified, which is achieved by extending the angle variable θ to the complex plane as $\theta = \xi + \mathrm{i}\eta$. Note that the complexified initial manifold E is locally two-dimensional.

The resulting expression of the semiclassical propagator takes the form as

$$\langle q|\hat{U}^n|E\rangle \simeq \sum_{\gamma} A_\gamma \exp\left(\mathrm{i}\frac{S_\gamma}{\hbar} - \mathrm{i}\frac{\pi}{2}\mu_\gamma\right), \tag{22}$$

where the sum γ is taken over all classical paths starting at the initial manifold E and ending at the final position q. A_γ and S_γ stand for the amplitude factor and the classical action for the classical orbit γ, respectively, obtained by inserting the path of each orbit. μ_γ represents the associated Maslov index.

IV. ERGODICITY IN THE COMPLEX SPACE

As mentioned in Sec. I, transport between classical forbidden regions can be achieved only using the complex orbits. The instanton allows the tunneling transition between the regions separated by the potential barrier. However, the situation to which the instanton method can be applied is limited at most to one- or multi-dimensional integrable systems [59].

Before developing the semiclassical argument, we show the nature of the complex classical dynamics in our classical map (2). In particular, we show that the dynamics in the complex plane exhibit ergodicity even though the phase space in the real plane separates into disjoint ergodic components. This is a key to understanding the step structure observed in the tunneling tail. It is also crucial to distinguish quantum tunneling in nonintegrable systems from that in integrable systems.

We will claim the ergodicity of the dynamics in the complex plane, based mainly on rigorous results for polynomial maps and numerical results for the maps involving transcendental functions, including the form of our potential (5). Ergodicity in the complex plane has also been studied numerically for the standard and semistandard maps [60,61]. We expect that a similar scenario holds for continuous flow systems, but it would be a much harder task to claim this fact even numerically.

A. Julia sets in the complex dynamics

The ergodicity of complex dynamics has been rigorously proved in the class of polynomial diffeomorphisms [30–34]. There is a theorem by Friedland and Milnor [62] which claims that two-dimensional polynomial maps are conjugate to either (1) elementary maps, (2) affine maps, or (3) generalized Hénon maps. It was also shown that only the generalized Hénon map is nontrivial and chaos does not appear in other maps. Furthermore, the generalized Hénon map can be written as a composition of the Hénon maps. This means that the well-known Hénon map F [63], which has a standard form

$$F : \begin{pmatrix} x' \\ y' \end{pmatrix} = \begin{pmatrix} y \\ y^2 - bx + a \end{pmatrix}, \tag{23}$$

can be considered as the simplest two-dimensional polynomial map. Note that the parameter a controls the dynamics: for $a \gg 1$ the complete horseshoe is realized [64], while for $a \simeq 1$ KAM curves appear and the phase space becomes a mixture of regular and chaotic regions. Here we assume that $|b| = 1$ since we are interested in the area-preserving case.

The map F can be straightforwardly extended from $F : \mathbb{R}^2 \to \mathbb{R}^2$ to $F : \mathbb{C}^2 \to \mathbb{C}^2$, and we can analyze the dynamics in the complex plane. In contrast to the dynamics in the real plane, the most important classification of the orbits is whether they stay in a finite region or go to infinity in time. We introduce the sets

$$I^{\pm} = \left\{(x,y) \in \mathbb{C}^2 \,|\, \lim_{n\to\infty} F^{\pm n}(x,y) \to \infty \ (n \to \infty)\right\}, \tag{24}$$

$$K^{\pm} = \left\{(x,y) \in \mathbb{C}^2 \,|\, \lim_{n\to\infty} F^{\pm n}(x,y) \text{ is bounded in } \mathbb{C}^2\right\}. \tag{25}$$

Since the Hénon map F is invertible, the dynamics can be defined in the backward direction. Thus, we can consider asymptotic behavior of dynamics in the backward direction as well.

Using the set $K^{\pm}$ of the bounded orbits, we introduce

$$K = K^{+} \cap K^{-}, \tag{26}$$

$$J^{\pm} = \partial K^{\pm}, \tag{27}$$

$$J = J^{+} \cap J^{-}. \tag{28}$$

Here K, $J^{\pm}$, and J are respectively called the filled Julia set, forward (resp. backward) Julia set, and Julia set.

B. Ergodicity and mixing in the potential theoretic Julia set

For the forward (resp. backward) Julia set $J^{\pm}$, we have *Theorem (Bedford-Smillie [30])*

$$\operatorname{supp} \mu^{\pm} = J^{\pm}. \tag{29}$$

Here

$$\mu^{\pm} \equiv \frac{1}{2\pi} dd^{c} G^{\pm} \tag{30}$$

denotes the (1,1)-current induced by the Green function $G^{\pm}(x, y)$ defined by

$$G^{\pm}(x, y) \equiv \lim_{n\to+\infty} \frac{1}{2^{n}} \log^{+} \|F^{\pm n}(x, y)\|, \tag{31}$$

where $\log^{+} t := \max\{0, \log t\}$ and the operator dd^{c} is defined by

$$dd^{c} \equiv 2\mathrm{i} \sum_{j,k=1}^{2} \frac{\partial^{2}}{\partial z_{j} \partial \bar{z}_{k}} dz_{j} \wedge d\bar{z}_{k} \tag{32}$$

is an analog of the Laplacian in two-dimensional real variables.

The current is a generalization of distributions or measures. This is analogous to the fact that distributions are a generalization of functions. Equation (30) has the same form as the Poisson equation in electromagnetism, where $\mu^{\pm}$ are the induced densities and the functions $G^{\pm}(x, y)$ are the associated Green functions.

The above theorem is a multidimensional analog of the relation $\operatorname{supp} \mu(z) = J_{P}$ established by Brolin for one-dimensional maps [65]. In the case of one-dimensional maps, $\mu(z)$ is induced by the Green function $G(z)$, which is defined in a similar way as above. Note that $\mu(z)$ for one-dimensional maps provides an equilibrium measure for which ergodicity or mixing can be shown to hold. On the other hand, $\mu^{\pm}$ in (30) are the currents, not the measures, so one cannot ask about ergodicity or mixing on $\mu^{\pm}$. A counterpart of the equilibrium measure $\mu(z)$ in two-dimensional maps is obtained by taking the wedge product as

$$\mu = \mu^{+} \wedge \mu^{-}, \tag{33}$$

which has been shown to follow the definition of the measure [34]. We denote the support of this measure μ by

$$J^{*} = \operatorname{supp} \mu. \tag{34}$$

J^{*} is called the *potential-theoretic Julia set*.

Using the the so-called convergence theorem of currents [31], we finally find the following properties for the complex Hénon map F.
Theorem (Bedford-Smillie [30–33])

(1) The measure μ is mixing and hyperbolic.

(2) For any unstable periodic orbit $\mathfrak{p}$, $\overline{W^{s}(\mathfrak{p})} = J^{+}$ and $\overline{W^{u}(\mathfrak{p})} = J^{-}$ hold.

Here $W^{s}(\mathfrak{p})$ and $W^{u}(\mathfrak{p})$ are the stable and unstable manifolds associated with the unstable periodic orbit $\mathfrak{p}$. The measure μ is said to be hyperbolic if the Lyapunov exponents Λ_{1} and Λ_{2} associated with μ satisfy $\Lambda_{1} > 0 > \Lambda_{2}$.

From the first statement, we can say that the system is chaotic in the set supporting the invariant measure μ. On the other hand, the orbits outside the set J^{*} cannot be chaotic. Ergodicity also follows immediately from the first statement. Note that the theorem does not specify the condition for the nonlinear parameter a in the Hénon map F, which means that the theorem holds even when regular and chaotic orbits coexist in real phase space. All these properties hold only for uniformly hyperbolic parameter regimes when restricted to dynamics in the real plane.

The above potential theory of complex dynamics is a powerful tool for studying the ergodic behavior of dynamics in the complex plane. Note, however, that these statements leading to mixing and ergodicity are given by the equilibrium measure μ and the associated potential-theoretic Julia set J^{*}.

On the other hand, numerical observations are usually made by iterating the orbits, so that the filled Julia set $K = K^{+} \cap K^{-}$ or the Julia set $J = J^{+} \cap J^{-}$ is more directly accessible than the potential-theoretic Julia set J^{*}. It is known that $J^{*} = J$ holds if the Hénon map is uniformly hyperbolic [32], but the best known result in the nonhyperbolic situation is that

$$J^{*} \subset J. \tag{35}$$

If the two sets do not coincide, then it is possible that there are points in the set J such that they do not have ergodicity. Therefore it is important to see the relation between the sets J and J^{*} in the case where uniform hyperbolicity does not hold. If they represent the same set, it turns out that the orbits in the complex plane can reach everywhere in the Julia set. In Sec. IV F, we will present a numerical result for the Hénon map suggesting that $J^{*} = J$ is a reasonable hypothesis even in mixed situations. Recall that a necessary condition for the complex orbits to contribute to the semiclassical propagator is that they are contained in the forward Julia set J^{+} [36,37].

The second statement of the above theorem is also helpful for our understanding of the dynamics in the complex plane. To explain what the properties $\overline{W^{s}(\mathfrak{p})} = J^{+}$ or $\overline{W^{u}(\mathfrak{p})} = J^{-}$ mean, let us consider the situation where regular and chaotic regions coexist in the real phase space.

Suppose the two distinct unstable periodic points, say, $\mathfrak{p}$ and $\mathfrak{p}'$, lie in the real plane but are separated by KAM curves. Obviously, two chaotic regions in the vicinity of $\mathfrak{p}$ and $\mathfrak{p}'$ do not communicate with each other within the real dynamics. However, the above theorem guarantees that there exist orbits initially placed in a neighborhood of $\mathfrak{p}$ that can access a neighborhood of $\mathfrak{p}'$ through the complex plane.

To see this, we first recall that $W^{s}(\mathfrak{p})$ and $W^{s}(\mathfrak{p}')$ are different invariant sets if $\mathfrak{p} \neq \mathfrak{p}'$, which means that the forward Julia set J^{+} contains, possibly a bunch of, points other than the points in the stable manifolds. Suppose that an initial condition $\mathfrak{q}$ is chosen in such a way that $\mathfrak{q} \in J^{+}$ but $\mathfrak{q} \notin W^{s}(\mathfrak{p})$. Since $\overline{W^{s}(\mathfrak{p})} = J^{+}$, the iterated points $F^{n}(\mathfrak{q})$ come close to and pass by the point $\mathfrak{p}$. At the same time, however, since

$\mathfrak{q} \in J^+ = \overline{W^s(\mathfrak{p}')}$, the point $\mathfrak{q}$ also approaches $\mathfrak{p}'$. The initial point $\mathfrak{q}$ should be complex, otherwise the orbit can only wander in a region bounded by KAM curves. In this way, one can see that the regions around unstable periodic points, although they are separated by KAM curves in the real plane, are connected via complex space.

C. Interior points of the filled Julia set and Siegel ball

If the sets $K^\pm$ have no interior points, then $\mathrm{vol}(K) = \mathrm{vol}(K^+ \cap K^-) = 0$ immediately follows. Here $\mathrm{vol}(K^\pm)$ denotes the four-dimensional volume (Lebesgue measure) of $K^\pm$ in $\mathbb{C}^2$. In this case, by definition, $K^\pm = J^\pm$ and $K = J$ holds. This means that all orbits that remain in a finite region, including KAM curves, are contained in J. Therefore, if $J^* = J$ holds even for mixed systems, KAM curves turn out to be contained in the set with hyperbolicity and mixing property.

If the Jacobian determinant of the Hénon map is not unity, i.e., $|b| \neq 1$, rigorous results are known: (1) $\mathrm{vol}(K^+) = 0$ for $|b| > 1$ and (2) $\mathrm{vol}(K^+) = 0$ or ∞ for $|b| < 1$ [34]. The inverse of the Hénon map is also the Hénon map with Jacobian determinant $1/|b|$, so the above results hold for the four-dimensional volume of K^- with Jacobian determinant $1/|b|$. On the other hand, for $|b| = 1$, which is our main concern, a rigorous result tells us only that $\mathrm{vol}(K^\pm) < \infty$.

As explained below, some speculation on the linearization around an elliptic fixed point suggests that $\mathrm{vol}(K) = 0$. It is well known that rotational domains appear when linearization around a neutral fixed point is achieved in the case of one-dimensional maps [66,67]. Neutral fixed points are those points for which the associated stability is unity, i.e., neither attracting nor repelling. When a neutral fixed point is linearizable, the so-called *Siegel disk* appears around the neutral fixed point [68]. Siegel disks occupy a positive area in $\mathbb{C}$, and so the filled Julia set K has a positive interior if the Siegel disk appears.

Linearization around a fixed point is also an issue in higher-dimensional complex maps. In the standard procedure for finding a transformation that provides linearization, the so-called *nonresonant condition* is required when constructing the perturbation expansion around the fixed point [66]. However, for the eigenvalues of the linearized matrix around an elliptic fixed point in the area-preserving map, there always appears a pair of eigenvalues $e^{i\kappa}$ and $e^{-i\kappa}$ with $\kappa \in \mathbb{R}$, which obviously violates the nonresonant condition. Therefore, it is impossible to proceed along with the standard procedure of linearization, and thus there is no chance to have Siegel balls, the higher-dimensional version of Siegel disks, around an elliptic fixed point.

D. Complexified real KAM curves

As for the rotational domain in the area-preserving map, the set of KAM curves could be a candidate in the area-preserving map. For a given angular frequency $\widetilde{\omega}$, the motion on the KAM curve, denoted by $\mathcal{C}_{\widetilde{\omega}}$, is expressed as a constant rotation using an appropriate coordinate, say, φ, as

$$\sigma : \varphi \mapsto \varphi + 2\pi\widetilde{\omega} \pmod{2\pi}. \tag{36}$$

To find such a coordinate φ, the conjugation function h is introduced, and it should satisfy the functional equation, $\sigma(h(p, q)) = h(F(p, q))$. The functional equation could be solved, for example, by assuming the form of the Fourier series [69]

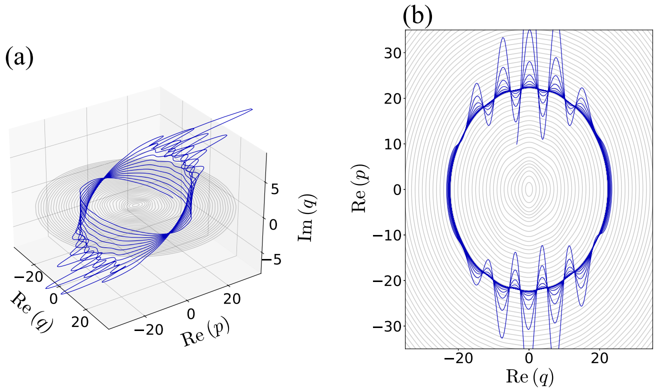

FIG. 7. An example of CRK. (a) Projection onto the $(\mathrm{Re}\, q,\ \mathrm{Re}\, p,\ \mathrm{Im}\, q)$ space. (b) Projection onto the $(\mathrm{Re}\, q,\ \mathrm{Re}\, p)$ plane. The parameters are set to $\tau = 0.01$, $\varepsilon = 1.0$, and $\lambda = 1.2$.

$$h(\varphi) = \sum_{m=-\infty}^{+\infty} h_m e^{im\varphi}. \tag{37}$$

If such a series has a positive radius of convergence in the complex φ variable, then the corresponding invariant curve with a given angular frequency $\widetilde{\omega}$ survives in the real plane. A positive radius of convergence implies that the corresponding KAM curves exist not only in the real but also in the complex plane. The motion on the resulting curve is also expressed as a rotation (36) with the same angular frequency $\widetilde{\omega}$ in the φ coordinate. Hereafter, we call the set of such closed curves *complexified real KAM curves* (CRK), meaning that the curves are obtained by complexifying the conjugate function $h(\varphi)$ associated with a real KAM curve. Since the orbits on the KAM curves, either in $\mathbb{R}^2$ or in $\mathbb{C}^2$, are bounded as $n \to \pm\infty$, they are by definition contained in $K = K^+ \cap K^-$.

An example of CRK is shown in Fig. 7. This was not direclty obtained by calculating the conjugate function $h(\varphi)$, but by iterating an orbit starting from a point sufficiently close to the real plane. As confirmed in Ref. [38], if the real phase space is almost covered by the KAM curves, the orbits started in this way follow the CRK well. The orbit, initially close to the real plane, spirals up in a small interspace between successively aligned cylindrical walls formed by a series of CRK obtained by scanning the imaginary angle $\mathrm{Im}\, \varphi$. Such a spiral motion along a bundle of CRK curves is a typical behavior observed for orbits in the complex plane. The orbit eventually reaches a certain imaginary region and forms a wavy circle there (see Fig. 7). This wavy pattern is an indication that the natural boundary of the conjugation function $h(\varphi)$ is nearby. The natural boundary is a superposition of many more wave components, typically of a fractal nature [69–72].

E. Complexified complex KAM curves

Invariant circles are not necessarily associated with the KAM curves in the real plane. To see this, we consider the case with $\varepsilon = 0$ in the potential function (5). In this case,

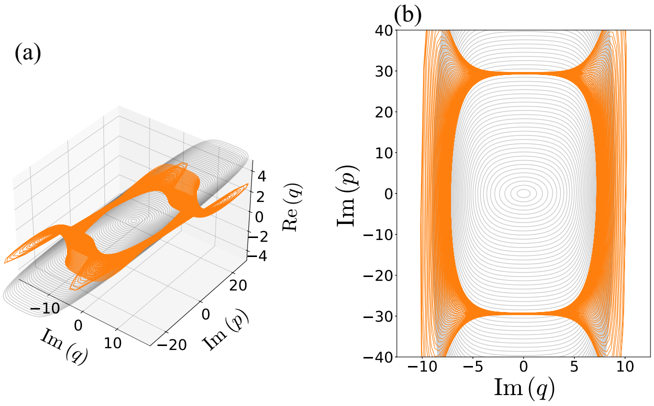

FIG. 8. An example of CCK. (a) Projection onto the ($\mathrm{Im}\, q$, $\mathrm{Im}\, p$, $\mathrm{Re}\, q$) space. (b) Projection onto the ($\mathrm{Im}\, q$, $\mathrm{Im}\, p$) plane. The parameters are set to $\tau = 0.01$, $\varepsilon = 1.0$, and $\lambda = 1.2$.

the map is simply reduced to the discrete linear oscillator,

$$f_{\mathrm{linear}} : \begin{pmatrix} q \\ p \end{pmatrix} \mapsto \begin{pmatrix} q + \tau p \\ p - \tau(q + \tau p) \end{pmatrix}. \tag{38}$$

The mapping relation (38) is nothing but the first-order symplectic integration of the harmonic oscillator $\mathcal{H}(q, p) = p^2/2 + q^2/2$, so the map f_{linear} preserves the quantity

$$E = \tfrac{1}{2}p^2 + \tfrac{1}{2}q^2 + \tfrac{1}{2}\tau q p. \tag{39}$$

For $E \in \mathbb{R}$, the orbits obviously move in the real plane. Note, however, that the value of E need not be real, but can be complex, i.e., $E = |E|e^{i\alpha}$ ($\alpha \in \mathbb{R}$). The constant of motion E makes sense for $E \in \mathbb{C}$, and the motion is confined by the complex-valued manifold. Note that the space $(E, \varphi) \in \mathbb{C}^2$ completely spans $\mathbb{C}^2$.

When ε becomes nonzero, the KAM scenario holds in the real plane, as explained. We may develop a similar argument not only in the real plane but also in the complex plane [73]. A simple way of looking at this is to perform a $\alpha = \pi/2$ rotation, that is, $q \to iq$ and $p \to ip$, which results in the same map (2) with the potential

$$\widetilde{V}(q) = \frac{1}{2}q^2 + 2\varepsilon \cosh\left(\frac{q}{\lambda}\right). \tag{40}$$

The pure imaginary plane $(q, p) \in i\mathbb{R}^2$ is thus an invariant plane under the map, and the orbits starting from it remain there. Although these invariant circles are not KAM curves in the standard terminology, we call these invariant curves *complex KAM curves* here. It is not clear whether or not the complex KAM curves exist not only in the pure imaginary plane $(q, p) \in i\mathbb{R}^2$, but also more generally in the complex plane [73]. If such complex KAM curves exist, we can also expect them to form a family of invariant circles as seen in the pure imaginary plane (see Fig. 8). We call them complex KAM curves as in the case of the pure imaginary plane.

If the complex KAM curves have the same origin as the real KAM curve, we can expect that *complexified complex KAM curves* (CCK) will also appear, based on a similar argument using the conjugate function for the real KAM curves. It would be difficult to construct the conjugate function in general, but we can provide numerical evidence for the existence of the CCK associated with the pure imaginary plane $(q, p) \in i\mathbb{R}^2$. Figure 8 shows an orbit moving along a set of closed curves in the pure imaginary plane, and it forms a cylindrical wall as in the case of the CRK (see Fig. 7). The CRK are associated with a real KAM curve as mentioned above, while the CCK are formed associated with a complex KAM curve.

We should note that the total dimension spanned by the rotational domains discussed here does not amount to the full dimension. First, for a given angular frequency $\widetilde{\omega}$, if the radius of convergence of the conjugate function $h(\varphi)$ is positive, the function $h(\varphi)$ can be analytically continued up to each natural boundary. As a result of the extension in the imaginary φ direction, we gain an additional dimension.

Second, the angular frequency of KAM curves has a positive Lebesgue measure in the angular frequency interval, so we gain another dimension in the angular frequency space, due to the KAM theorem. More precisely, this follows from the fact that the irrational numbers satisfying the Diophantine condition have a positive Lebesgue measure in the real numbers.

Third, we have a further extension in the α direction as performed above. It turns out that the total volume of the rotational domains including the complex KAM curves is less than four, since unperturbed invariant circles with rational angular frequencies are broken when the perturbation is added, and thus the Hausdorff dimension in the direction of the rotation number is less than one. This implies that the bundle of rotational domains associated with KAM curves does not occupy a four-dimensional volume. This speculation, together with the absence of the Siegel ball, suggests that the filled Julia $K = K^+ \cap K^-$ has an empty interior.

F. J and J^* for the Hénon map

Rigorous results for the Hénon map introduced in Sec. IV B imply ergodicity of the dynamics in the complex plane. The orbits are mixing and thus ergodicity follows on the potential-theoretic Julia set J^*. The argument developed in the last paragraph of Sec. IV B, based on the fact that $\overline{W^s(\mathfrak{p})} = J^+$ and $\overline{W^u(\mathfrak{p})} = J^-$ for any unstable periodic orbit $\mathfrak{p}$, suggests that any two regions are connected via the complex plane if the two regions contain unstable periodic orbits.

Here we provide further evidence that ergodicity in the complex plane is not a far-fetched hypothesis, but a rather reasonable one. The first observation is the comparison of J with J^* for the Hénon map. There may be several ways to visualize the Julia set in $\mathbb{C}^2$, for example, by taking a three-dimensional slice or projection onto a two- or three-dimensional plane. However, as discussed above, the Julia set is likely to have null four-dimensional volume. This means that a random sampling of the initial points in $\mathbb{C}^2$ will not hit the points on J. So we take a slice of J by an unstable manifold, because unstable manifolds are contained in J^- by definition, which restricts our sample space to a (locally) two-dimensional plane.

For this purpose, we introduce a local coordinate on the unstable manifold, which is expressed in terms of the

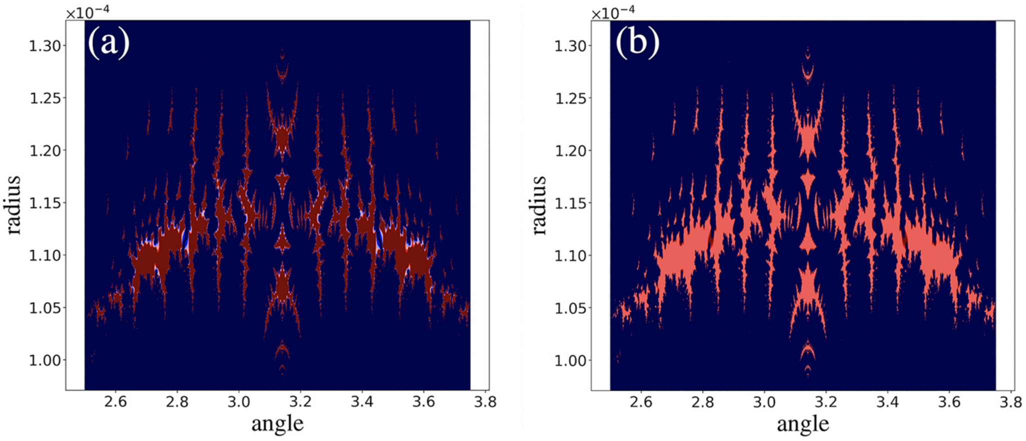

FIG. 9. (a) The intersection $W^u(\mathfrak{p}) \cap K^+$ between the unstable manifold of an unstable fixed point $(x, y) = (0, 0)$ for the Hénon map and the forward filled Julia set K^+. The plots are drawn in the coordinate plane (Θ, r) (see text). The colors reflect the number of time steps up to which the orbits leaving each point in this frame leave a properly chosen finite-sized box. The red regions show the set of initial points that remain in a finite region for a sufficiently long time, while the orbits in the blue region diverge to infinity in a relatively short time. (b) The Green function $G^+(x, y)$, which is evaluated numerically according to the definition (31). The parameters of the Hénon map (23) are set to $a = 0.8$ and $b = 1$.

coordinates in the radial and angle direction as

$$\begin{aligned}\{(\xi_x = r\cos\Theta, \xi_y = r\sin\Theta) \mid (\delta/\lambda) \leqslant r \leqslant \delta,\\ \Theta_1 \leqslant \Theta \leqslant \Theta_2\},\end{aligned} \tag{41}$$

where λ is the stability exponent for the unstable direction. The radial-angle coordinate is used to represent the Julia set on the unstable manifold.

If the orbits initially placed on the unstable manifold remain in a finite region as $n \to +\infty$, then these points are contained in the forward filled Julia set K^+. If $K^+ = J^+$ holds, then such orbits should be contained in the set $J = J^+ \cap J^-$. Note that it will be still be difficult to find the orbits that do not diverge to infinity, since a two-dimensional slice of J is expected to be an object whose dimension is less than one if $K^+ = J^+$ holds.

Figure 9 plots the intersection $W^u(\mathfrak{p}) \cap K^+$, where $\mathfrak{p}$ is an unstable fixed point of the Hénon map. The plot was obtained by counting the number of iterations up to which the orbits leaving each point in this frame leave a properly chosen box of finite size. Thus, the plot can be considered as an approximation of $W^u(\mathfrak{p}) \cap K^+$. By increasing the iteration step, we can observe that all points eventually diverge to infinity and do not stay in a finite region, even though the escaping rate from a finite region is extremely slow. This is also another numerical proof that the set K^+ does not have a finite four-dimensional volume. As can be seen, the set K^+, as well as the set J^+, exhibits a fractal structure, which is a typical signature of the Julia set in one-dimensional complex maps [74].

We show the Green function $G^+(p, q)$ in Fig. 9(b) using the local coordinate introduced above. Here the Green function $G^+(p, q)$ is numerically evaluated according to the definition (31). As explained above, the support of the Green function $G^+(p, q)$ is the set J^+. We can see that the finite-step approximation of J^+, shown in Fig. 9(a), gives a similar profile to the support of $G^+(p, q)$, shown in Fig. 9(b). This result therefore suggests that $J = J^*$ holds even if the phase space is a mixture of regular and chaotic orbits and the system is not uniformly hyperbolic.

G. Ergodicity in the complex plane for the ultra-near integrable system

Next, we examine the ergodicity for the map under consideration. The formulation based on the Green function is available only in the case where the map is expressed as polynomial functions. This is because the normalization, which is achieved by the factor $1/2^n$ in Eq. (31), is not available if the map contains transcendental functions. Hence, we perform brute-force numerical experiments to verify the ergodicity here.

Since our current interest is in the transition from the classical manifold supporting the quantum initial wave packet $|\psi_0\rangle$, we focus on the transitivity of the orbit starting from the manifold specified by the action E, which is more explicitly specified by the rotated ellipse Γ given in Eq. (20).

Here we focus on the orbits starting from the initial manifold, which is specified by the coordinate (E, θ), and tending towards the real KAM or complex KAM curves. The latter is chosen here as the pure imaginary plane. As explained above, the orbit comes close to a family of CRK or CCK and then spirals down to the associated real or complex KAM curve. Figure 10(a) shows the initial value plane $\theta = \xi + i\eta$, on which we place the colors representing the radius of the real KAM curves to which the orbits first tend. The radius of each KAM curve is measured using the coordinate of the position where the corresponding real KAM curve intersects. Figure 10(b) is a magnified plot of Fig. 10(a), whereas Fig. 10(c) shows a part of the initial conditions that first approach the CCK curves associated with the $(\mathrm{Im}\, q, \mathrm{Im}\, p)$ plane. In the latter case, the radius of the KAM curves is also measured using the coordinate of the position where the associated complex KAM curve intersects. Note that the set of initial conditions associated with the CCK [see Fig. 10(c)] is located around $\xi = \pi/2$ or $3\pi/2$. The positions are shifted

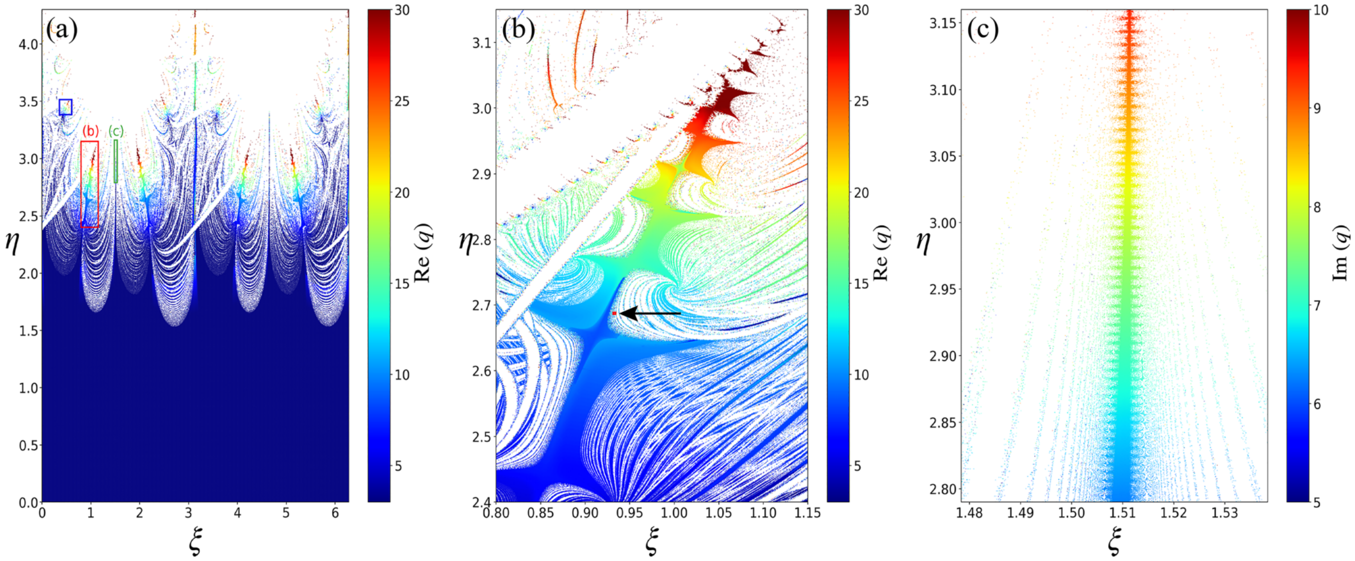

FIG. 10. (a) The color plot of the radius of the real KAM curves that the orbits first approach. The part indicated by the blue box at the upper left is referred to in Fig. 15. (b) Magnification of the part indicated by the red box in plot (a). The small red box with the arrow indicates the area that is magnified to show the hierarchical structure in Fig. 12(a). (c) Magnification of the area indicated by the green box in plot (a). In plot (c) we place the colors representing the radius of the imaginary KAM curves to which the orbits first tend. The parameters are set to $\tau = 0.01$, $\varepsilon = 1.0$, and $\lambda = 1.2$.

exactly by $\pi/4$ in the ξ direction from the position for the CRK. In other words, the initial conditions for CRK and CCK are found in the (ξ, η)-plane with different values of ξ.

These figures tell us that the target KAM curves change continuously as one varies the initial condition, meaning that the orbits on the initial manifold can transfer to any KAM curves, either in the real or imaginary plane. The initial manifold chosen here is nothing special, so this result suggests ergodicity in the complex plane. Moreover, as plotted in Fig. 12(a), if we zoom in some spots, we can find a similar color pattern, which implies that the observed structure is self-similar and hierarchical.

After approaching the real (resp. imaginary) plane, the orbits spiral up along the family of CRK (resp. CCK) associated with a real (resp. imaginary) KAM curve that the orbits first approach. Then they switch to another CRK (or

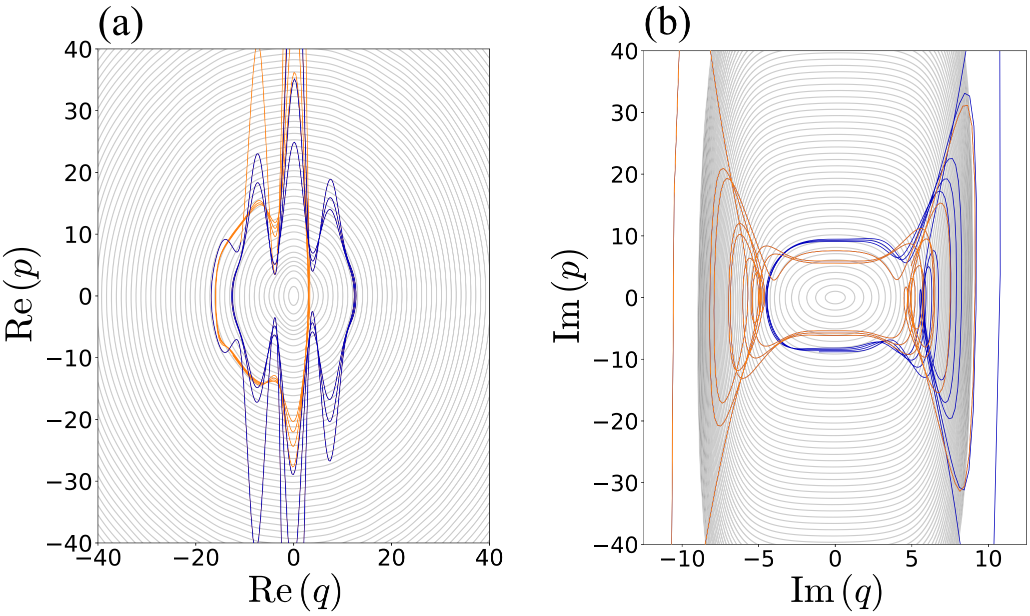

FIG. 11. An example of the orbit that first rotates around a set of CRK (blue) and then switches to a set of CCK (orange). (a) Projection onto the $(\mathrm{Re}\, q, \mathrm{Re}\, p)$ plane. (b) Projection of the same orbit onto the $(\mathrm{Im}\, q, \mathrm{Im}\, p)$ plane. The parameters are set to $\tau = 0.01$, $\varepsilon = 1.0$, and $\lambda = 1.2$.

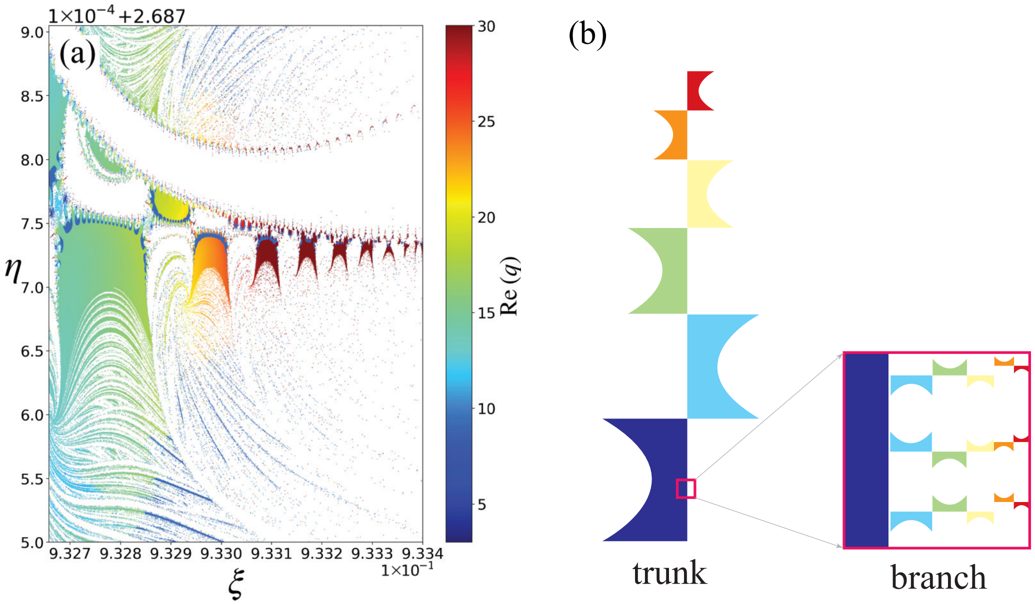

FIG. 12. (a) The area that enlarges the small red box indicated by the arrow in Fig. 10(b). (b) Illustration of the hierarchical structure. The vertically aligned structure on the left side represents the trunk shown in Fig. 10(b). The horizontally aligned structures in the right box represent the branches growing from the trunk, and one such branch structure is shown in plot (a).

CCK) and start spiraling down again. An orbit exhibiting such behavior is shown in Fig. 11. Figure 11(a) and 11(b) show the orbits projected on the (Re q, Re p) plane and the (Im q, Im p) plane, respectively. The orange and blue parts represent the spiral motion along the CRK and CCK curves, respectively. In this case, the orbit first rotates around a CRK and then switches to a CCK. On the other hand, an orbit shown in Fig. 14(b) exemplifies the case where the transition occurs from one CRK to another CRK. These observations also confirm the transitivity of the orbits in the complex plane.

V. IMAGINARY ACTION OF COMPLEX PATHS AND THE PLATEAU AMPLITUDE

A. Classification of the type of the orbits

As confirmed in the previous section, the orbits in the complex plane explore the set J in an ergodic way, so that the orbit initially placed on the initial manifold Γ can come close to arbitrary real KAM curves. The question we have to ask then is which complex orbits give the most dominant contribution to the semiclassical propagator (17). The magnitude of each contribution in the semiclassical sum (22) is determined by the amplitude factor and the magnitude of the imaginary part of the action (imaginary action, for short). Of these, we focus on the imaginary action because it controls the order of magnitude of the tunneling tail. The amplitude factor could come into play, especially if one needs to examine the balance between the number of contributing orbits and each weight associated with the amplitude factor, but we will not develop such a detailed argument here, just try to find a rough estimate in terms of the imaginary action.

To do this, we first classify the type of complex orbits according to their itinerary in the complex plane. As explained in the previous section, the orbits spend most of their time along either the CRK or the CCK. They exhibit spiral motions along them unless they are exactly on the KAM curves. Therefore, it makes sense to classify the type of orbits according to whether they are along the CRK or along the CCK. Note that the initial manifold Γ is close to the former type of orbits.

Figure 7 displays the case where the orbits first move to the CRK, while Fig. 8 gives the case corresponding to the CCK. As remarked above, these two types of orbits are found in separate regions of the (ξ, η)-plane. In the course of time, the orbits once moving along a set of CRK curves may jump to other CRK or CCR curves and vice versa, as shown in Fig. 11. Thus, we need to further classify the orbits according to which complexified KAM curves the orbits approach after moving once along a complexified KAM curve.

The itinerary of the orbits is encoded in the hierarchical structure in the (ξ, η)-plane. Figure 12(a) gives the area that enlarges the small red box pointed by the arrow in Fig. 10(b). The main trunk, shown in Fig. 10(b), represents the orbits that jump directly to the target CRK, and the higher-order branches, shown in Fig. 12(a), represent the orbits that stop over several CRKs before reaching the target. Figure 12(b) illustrates the hierarchical structure in the (ξ, η)-plane. Similar tree structures appear in the case of CCK, although not shown here.

B. Imaginary action of roundabout paths

The classical action (18) is given as a sum over intermediate variables. So we can expect that the longer the detour, the larger the imaginary action will be. In particular, if the orbit once travels along a set of the CCK and returns to another set of the CRK, it gains an extra imaginary action, resulting in a smaller contribution to the semiclassical propagator.

Before examining roundabout paths, we confirm that the orbits associated with the CCK do not qualify as candidates

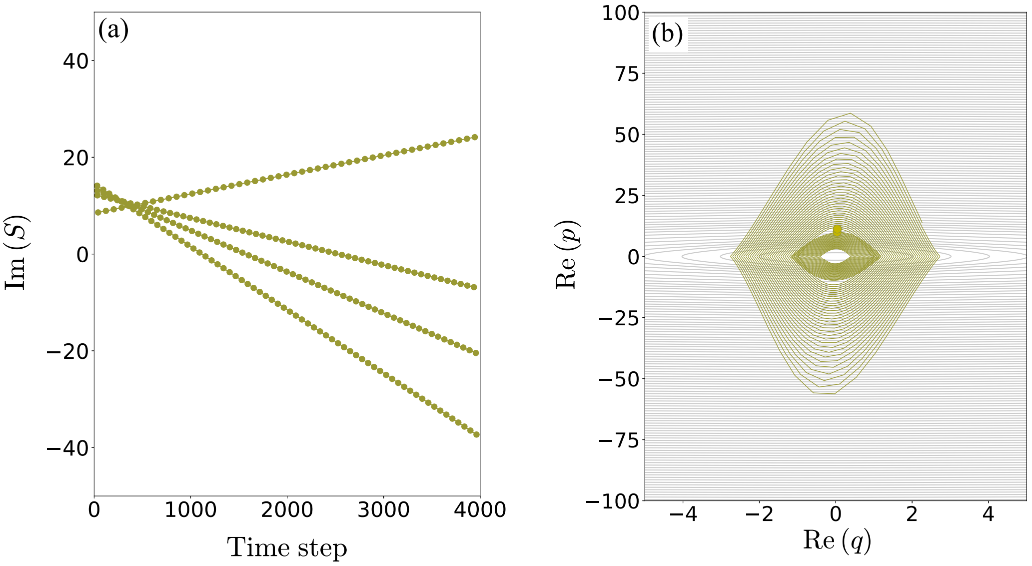

FIG. 13. (a) The variation of the imaginary action for the case where the initial conditions are chosen from the plot shown in Fig. 10(c). The dot is plotted at each time when the condition Im $q_n = 0$ is satisfied. (b) The projection onto the (Re q, Re p) plane of the two of the orbits used to plot (a). One rotates in an outer region, while the other rotates in an inner region. The initial conditions of these two orbits are close to each other and are represented by the dot. The parameters are set to $\tau = 0.01$, $\varepsilon = 1.0$, and $\lambda = 1.2$.

for the semiclassical contribution. In Fig. 13 we show the behavior of the imaginary action and the projection of the orbits onto the (Re q, Re p) plane, respectively. Several representative initial conditions are chosen from the plot in Fig. 10(c). As can be seen in Fig. 13(a), the imaginary actions do not remain constant, but increase or decrease monotonically. This behavior is in sharp contrast to that found for the orbits associated with the CRK (see Figs. 14 and 15). In addition, Fig. 13(b) clearly shows that the orbits projected onto the (Re q, Re p) plane obviously deviate from the real KAM curves, since they rotate around the CCK and do not approach the real KAM curves. For these reasons, we can conclude that the orbits associated with the CCK do not need to be taken into account.

As for the orbits starting from the side branches in the hierarchical tree structure, the associated imaginary action is larger than that for the main trunk as shown in Fig. 14(a). The imaginary action of the orbit starting from the trunk quickly reaches almost the final value. On the other hand, the imaginary action for the orbit leaving a branch in the hierarchical structure takes a rather small value for a while, then it gives a value that is larger than the imaginary action obtained for

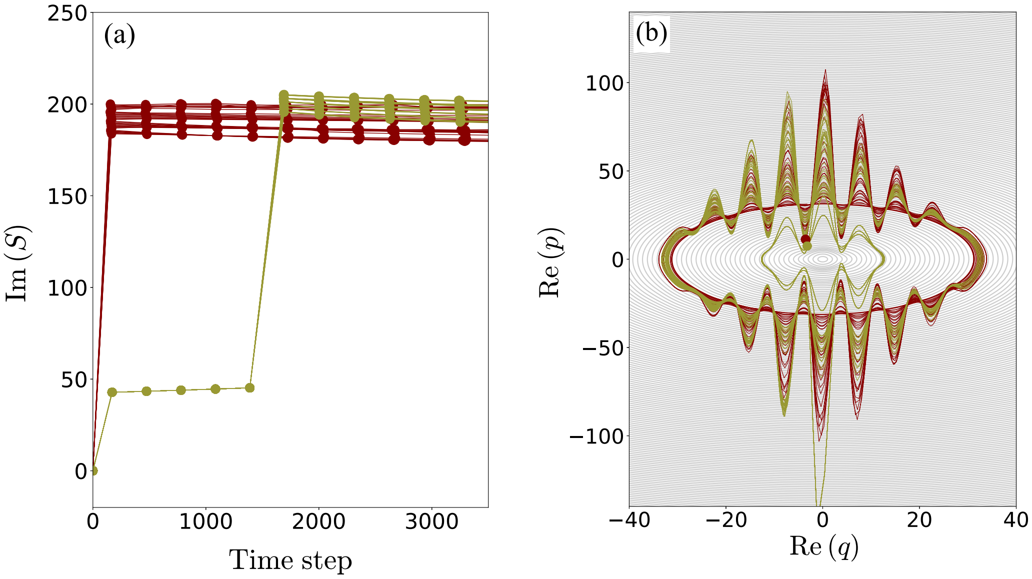

FIG. 14. (a) The variation of the imaginary action for the case where the initial condition is taken from the main trunk shown in Fig. 10(b) (red) and the case where it is taken from a higher order branch shown in Fig. 12(a) (yellow). (b) The projection onto the Re p-Re q plane of the orbits used to plot (a). The red and yellow dots placed around the center of the plot indicate the initial points. Note that the target real KAM curves are almost the same for both cases. The parameters are set to $\tau = 0.01$, $\varepsilon = 1.0$, and $\lambda = 1.2$.

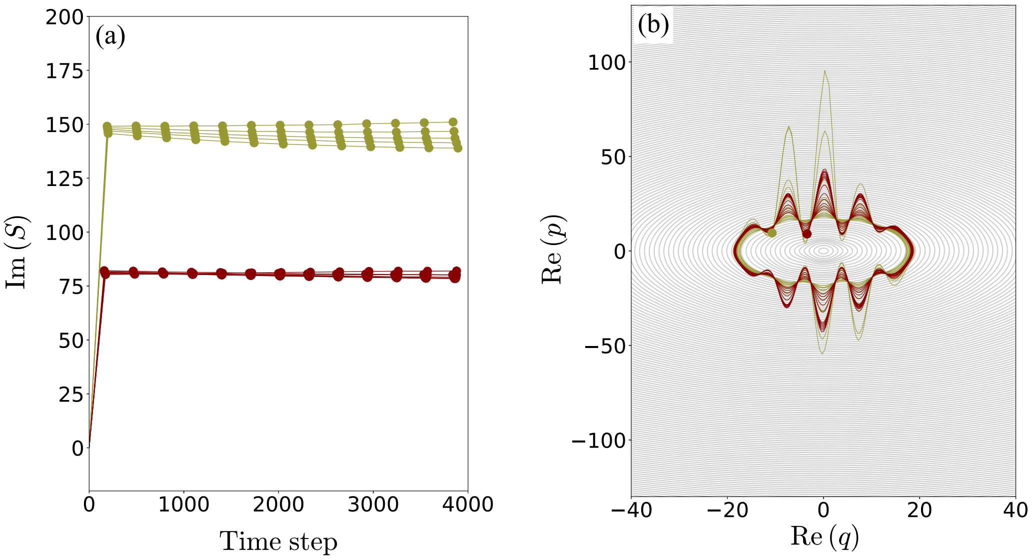

FIG. 15. (a) The variation of the imaginary action for the cases where the initial conditions are chosen from the main trunk with smaller values of η (red) and larger values of η (yellow). The former is taken from the point in Fig. 10(b), while the latter is taken from the point in the blue box in Fig. 10(a). So the value of η is smaller in the former case than in the latter. (b) The projection onto the (Re p, Re q) plane of the orbits used to plot (a). Note that the target real KAM curves are almost the same for both cases. The parameters are set to $\tau = 0.01$, $\varepsilon = 1.0$, and $\lambda = 1.2$.

the trunk orbit, although its final manifold is almost the same as that for the trunk orbit. This is also due to the fact that higher-order orbits make a detour before reaching the final real KAM curves. As can be seen in Fig. 14(b), the former orbit jumps directly to the final manifold, whereas the latter orbit rotates several times before reaching the final manifold. The latter orbit is temporarily trapped by an inner CRK, then it moves to the final manifold. This observation tells us that the relevant complex orbits that dominate the semiclassical propagator (22) are the orbits located in the main trunk in the hierarchical structure.

Notice that all the complex orbits do not necessarily contribute to the semiclassical propagator when applying the semiclassical approximation in the complex domain. This is because the so-called Stokes phenomenon occurs when applying the saddle point approximation [23–25,75,76]. A simple example of the Stokes phenomenon can be found in the evaluation of the Airy function using the saddle point method. The Stokes phenomenon also occurs when evaluating the multiple integral, but it is by no means trivial how to deal with the Stokes phenomenon for the integral with more than two saddles [77,78]. This is a central issue in recent developments in resurgent theory, and some attempts have even been made in chaotic systems [28,29]. However, we do not take such a sophisticated approach here, but simply observe the sign of imaginary action. Such a crude approach is justified by the fact that the complex orbits with negative imaginary actions give exponentially divergent contributions, which should be eliminated when evaluating the exponentially decaying tunneling tail. Therefore, we will treat the problem simply by neglecting the region where the resulting imaginary actions take negative values.

C. Complex orbits attaining the minimal imaginary action

We will further narrow down the candidate complex orbits. As shown in Fig. 10, there are not one but many trunks accompanying the hierarchical structure. Among them, the most dominant orbits are determined by the value of η, the depth of the initial position in the (ξ, η)-plane. Such a principle is generally valid not only for ultra-near integrable systems, but also for mixed systems, where chaotic regions are relatively large and visible [10,36–38].

As found in [38], the complex orbits departing from the position with smaller η give larger contribution in mixed systems. We have compared the imaginary action along the stable manifold associated with unstable periodic orbits in chaotic regions surrounding the regular region. The reason for focusing on stable manifolds is precisely the fact that $\overline{W^s(\mathfrak{p})} = J^+$ holds. It was also shown in [39] that the complex paths connecting the initial and final manifolds for the propagator are well approximated by the stable manifold over time.

Note, however, that there is an important difference between the situations examined here and in [38]. In the previous case, the complex orbits eventually approach real chaotic seas, while in the present case, the orbits repeat spiral-up and spiral-down motions and keep oscillating in the complex plane, as explained above. Despite this difference, it is common that the orbits with smaller η carry smaller imaginary actions and thus give larger contributions in the semiclassical sum. This can indeed be verified by plotting the imaginary action for the cases with different η. As shown in Fig. 15, the orbits leaving a trunk with smaller η gain smaller imaginary actions compared to the cases with larger η, even though the target real KAM curves for both cases are almost the same.

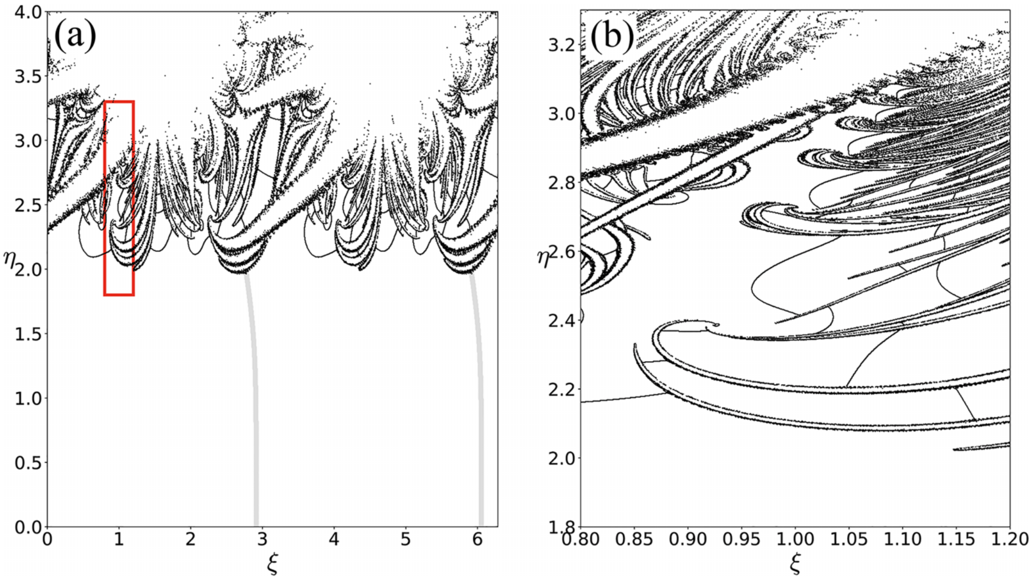

FIG. 16. The set $\mathcal{M}_N$ defined by (42). Plot (b) is a magnification of the area enclosed by the red square in plot (a). The gray curves in plot (a) attached to the ξ axis are called natural branches [9,10]. The parameters are set to $\tau = 0.05$, $\varepsilon = 1.0$, and $\lambda = 1.2$.

D. Complex orbits satisfying the boundary conditions

Now that we have information about which orbits have the smallest imaginary action, we examine whether these orbits can explain the step structures found in the time evolution of the wave packet, shown in Sec. II. Since we consider the propagator in the form (22), we have to consider complex orbits whose final q_n is real-valued. We also need to focus on the propagator at each time when the step structure appears in the time evolution. As shown in Fig. 6 and discussed in Sec. II, the step structure appears periodically with period $N/2 = E_{\rm ex}/E_0 = 63$. The factor 1/2 appears because we are looking at the absolute value.

Figure 16 plots the set of initial conditions satisfying $\mathrm{Im}\, q_N = 0$:

$$\mathcal{M}_N = \{\, q_0 = (\xi, \eta) \in \mathbb{C}^2 \,|\, (q_0, p_0) \in \Gamma,\ \mathrm{Im}\, q_N = 0 \,\}. \quad (42)$$

The plotted region is chosen to contain the region that gives the minimum imaginary action. Each string represents a single complex orbit satisfying the condition $\mathrm{Im}\, q_N = 0$, and the corresponding $\mathrm{Re}\, q_N$ runs from $-\infty$ to ∞ along the string.

Since we are interested in the amplitude of the time-evolved wave function at the position where the underlying real KAM curve supports the eigenstate excited by the resonance condition (12), we focus on the orbit satisfying the condition $\mathrm{Re}\, q_N = q^{\rm t}$, where $q^{\rm t}$ denotes the coordinate of the turning point obtained by projecting the associated real KAM curves onto the q axis.

Figure 17 shows the variation of $\mathrm{Re}\, q_n$ and $\mathrm{Im}\, q_n$ as a function of the time step. As expected, $\mathrm{Im}\, q_n$ is found to be zero when $\mathrm{Re}\, q_n$ is almost equal to the position $q^{\rm t}$ of the turning point. This period coincides with the period of oscillation of the step structure of the wave function (see Fig. 6). Therefore, it makes sense to evaluate the corresponding imaginary action at each point in time when the periodic oscillation occurs.

Figure 18 gives the behavior of $\mathrm{Im}\, S_n$, for which the two different KAM curves satisfying the resonance condition (12) are chosen as the final manifolds. The light blue curve shows the case where the final KAM curve is the support for the first excited state ($m = 1$) in Eq. (12), and the dark blue curve corresponds to the case for the second excited ($m = 2$) state. We can see that, at each time step where $\mathrm{Im}\, q_n = 0$, the value of $\mathrm{Im}\, S_n$ remains almost constant. The behavior of $\mathrm{Im}\, S_n$ is the same in the case where the value of η of the initial position is large (see Fig. 15), but the imaginary action thus obtained is larger and makes a smaller contribution, for the reason mentioned above.

As shown in Fig. 14, the orbits with larger imaginary action make a detour before reaching the target manifold, while the orbits with the smallest imaginary action jump directly to the final manifold. As shown in Fig. 14(a), the variation of $\mathrm{Im}\, S_n$ occurs in a very short time, which means that there is almost no “loss of imaginary action in the transition process. The wavy pattern of the final manifold appears, as explained in Sec. IV D, because the iterated orbits are close to the natural boundary. We notice that the initial condition for the orbit with the smallest imaginary action is located around the region where the wavy manifold bends most inward. It is as if the orbit was on the final manifold from the beginning.

We can understand the behavior of the most dominant complex path more clearly by observing the three-dimensional plot. As shown in Fig. 19, the most dominant path is located very close to or exactly on the wavy part of the final manifold from the beginning. It shows no detour, but jumps directly to the final manifold. After that it starts to spiral down to the real plane. In other words, the “shortest path” in terms of distance in the complex phase space gives the orbit with the minimal imaginary action, and this would be a principle specifying the most dominant complex path.

Figure 20 shows that the minimal imaginary action $\mathrm{Im}\, S$, evaluated according to the principle described above, reasonably well reproduces the squared magnitude $|\mathrm{Con}_k^{(M)}(q)|^2 =$

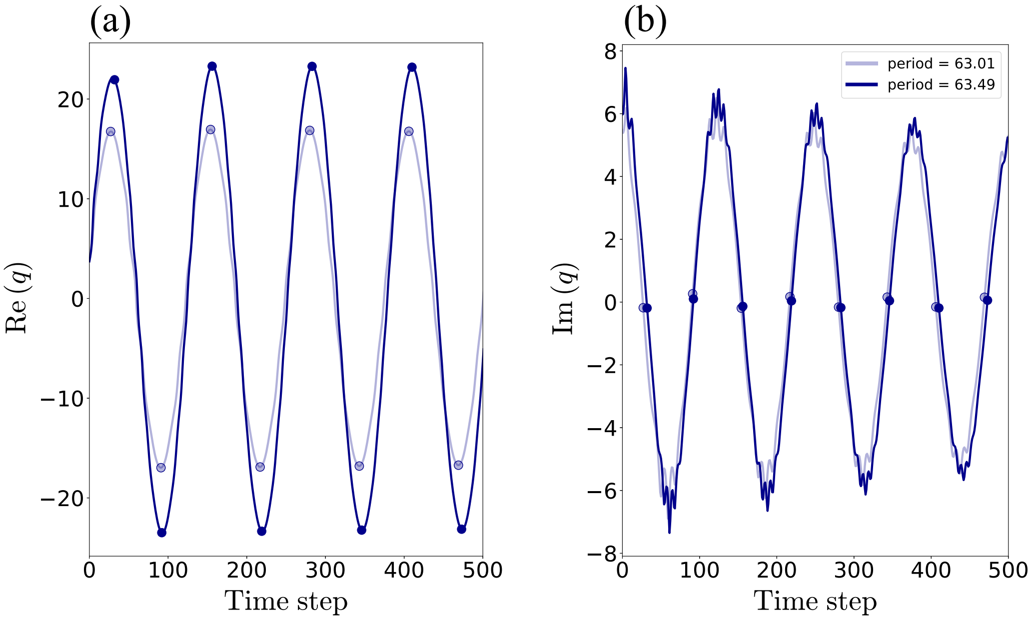

FIG. 17. The behavior of (a) Re q_n and (b) Im q_n for the orbits moving along the CRK. The light blue and dark blue curves show the cases where the orbits move along the CRK associated with the real KAM curve supporting the first resonance state [$m = 1$ in Eq. (12)] and the second resonance state ($m = 2$), respectively. The dots in the plot (a) indicate the points when Im $q_n = 0$ in plot (b). The parameters are set to $\tau = 0.05$, $\varepsilon = 1.0$, and $\lambda = 1.2$.

$|\langle q|\Phi_k^{(M)}\rangle\langle\Phi_k^{(M)}|\Psi_0\rangle|^2$ in the sum (13). The reason why the semiclassical prediction quantitatively overestimates the quantum calculation would be that we have given a rough estimate only using the imaginary action, without including the amplitude factor here. Another reason, which must be a major one, is that our initial condition $|\psi_0\rangle$ and the associated classical initial manifold Γ are too crude to approximate the ground state $|\Psi_0\rangle$. As found in Fig. 1, the classical invariant circles are deformed from the set of ellipsoidal curves Γ due to the second term in (5), so the support of the minimal wave packet does not approximate the underlying invariant curve supporting the ground state of the quantum map.

As can be seen in Fig. 2(a), the ground-state wave function $|\langle q|\Psi_0\rangle|^2$ of the quantum map coincides with that of the truncated quantum BCH Hamiltonian $\hat{H}_{q\text{BCH}}^{(M)}$ up to the first plateau. Recall that the part up the first plateau could be reproduced by the branches that are connected to the ξ axis, shown by gray curves in Fig. 16. These branches are

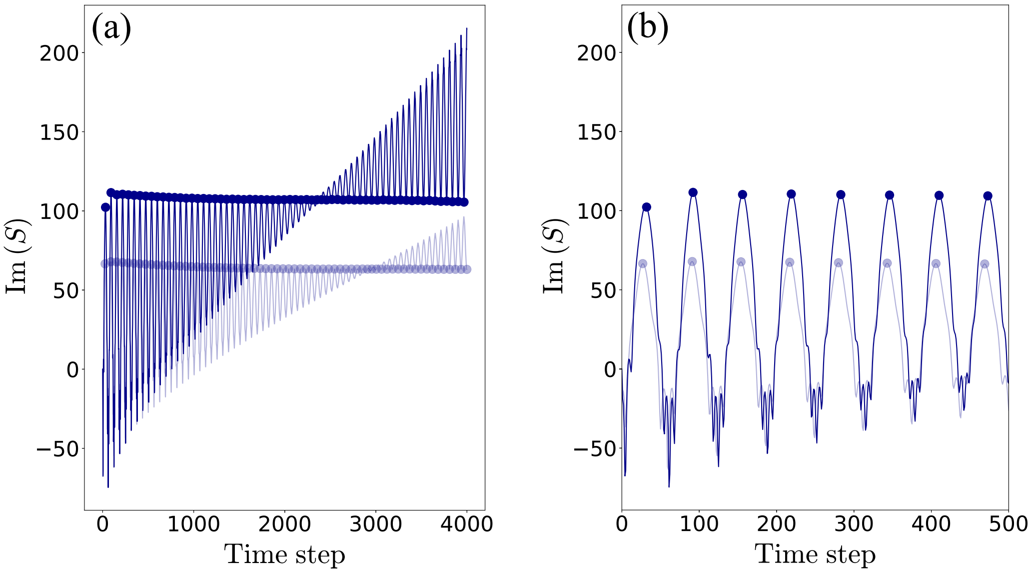

FIG. 18. The behavior of Im S_n for the orbits moving along the CRK. The light blue and dark blue curves show the cases where the orbits move along the CRK associated with the real KAM curve supporting the first resonance state [$m = 1$ in Eq. (12)] and the second resonance state ($m = 2$), respectively. Plot (b) is a magnification of plot (a). The dots indicate the points where the condition Im $q_n = 0$ is satisfied (see Fig. 17). The parameters are set to $\tau = 0.05$, $\varepsilon = 1.0$, and $\lambda = 1.2$.

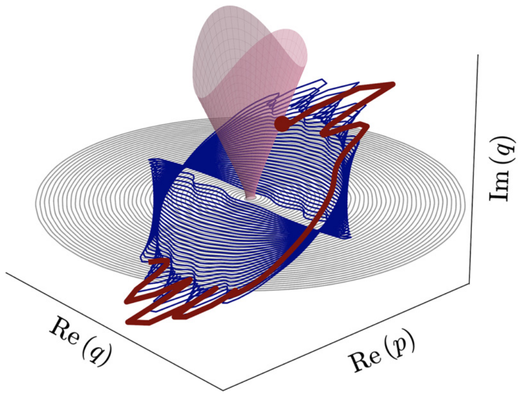

FIG. 19. Illustration of the complex path with the minimal imaginary action. The pink bottle-shaped manifold represents the initial manifold Γ. The red curve shows the complex path with the minimal imaginary action, which jumps to the final manifold colored in blue. The wavy pattern indicates that the CRK is close to its natural boundary. The complex path is captured by such a wavy part of the final manifold.

called *natural branches* in Refs. [9,10]. The points connected to the ξ axis correspond to the turning points of the KAM curves in the real plane. The natural branches are the complex paths that already exist in the integrable limit, so they can be regarded as an analog of the instanton. The result shown in Fig. 20 implies that, up to the first step, the complex orbits other than the natural branches do not manifest themselves in the amplitude of the wave function, although they have smaller imaginary actions. This must be due to the fact that the real actions $\mathrm{Re}\, S$ of these orbits are random and cancel with each other.

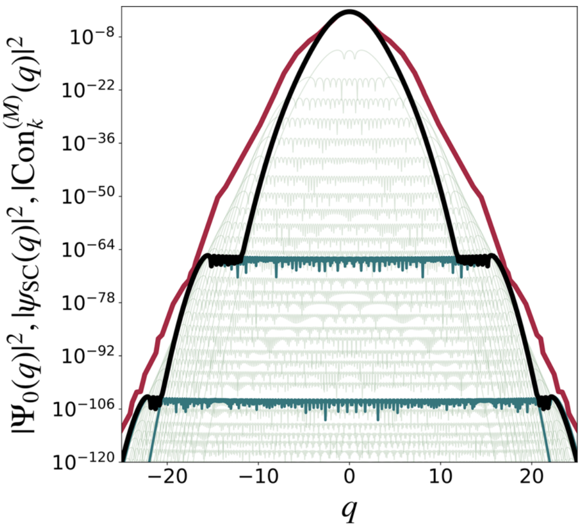

FIG. 20. Ground-state eigenfunction $|\langle q|\Psi_0\rangle|^2$ (black). Squared magnitudes $|\mathrm{Con}_k^{(M)}(q)|^2 = |\langle q|\Phi_k^{(M)}\rangle\langle\Phi_k^{(M)}|\Psi_0\rangle|^2$ in the sum (13) (light green). The resonance states $k = 125$ and $k = 251$ are shown in dark green, respectively. The red curve shows $|\psi_{\mathrm{sc}}(q)|^2 := \exp(-2|\mathrm{Im}\, S|/\hbar)$, where $\mathrm{Im}\, S$ is the minimal imaginary action evaluated according to the principle given in the text. The parameters are set to $\hbar = 1$, $\tau = 0.05$, $\varepsilon = 1.0$, and $\lambda = 1.2$.

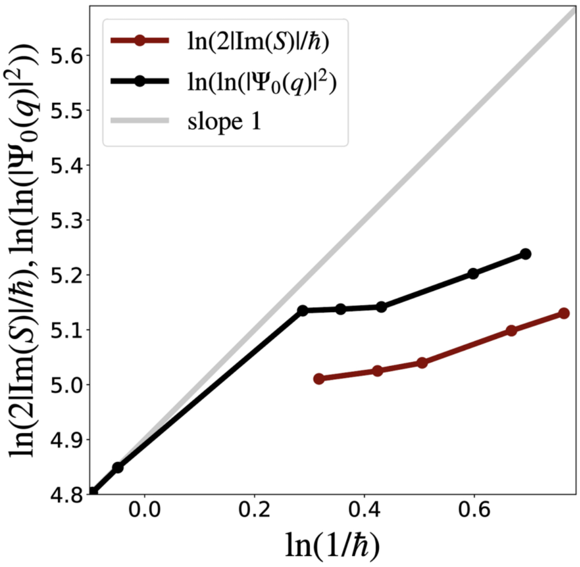

FIG. 21. The black curve shows the ground-state eigenfunction for the quantum map (4) and the red curve is obtained by the smallest imaginary action $\mathrm{Im}\, S$ (see text). The line with slope 1 is added for reference. The parameters are set to $\tau = 0.05$, $\varepsilon = 1.0$, and $\lambda = 1.2$.

On the other hand, at the plateau energy for which the resonance condition (12) is satisfied, the complex orbits contribute coherently due to the constructive interference, which will be explained in Sec. VI. The decay after the plateau, similar to the initial decay curve described by the natural branches, would be associated with the natural branches connected to the KAM curve supporting the first resonance state ($m = 1$).

The most important result would be that the minimal imaginary action $\mathrm{Im}\, S$ always takes lower values than the instanton action represented by the natural branches. This means that the enhancement of the tunneling probabilities occurs precisely because the transport is driven by the orbit in the Julia set. So far, the origin of the enhancement of tunneling probability in nonintegrable systems has been sought in several ways, but this is the first time, to the authors' knowledge, that its direct origin has been pointed out.

E. $\hbar$ dependence of the step height

We now recall that the position and height of the steps move as a function of $\hbar$, as shown in Fig. 4. The step appears on the KAM curve supporting the eigenstates that satisfy the resonance condition (12), so we can specify the $\hbar$ dependence of the step position. On the other hand, the dependence of the step height on $\hbar$ is not trivial. In fact, as demonstrated in the inset of Fig. 4, the stretched exponential growth appears when evaluating the step height at a fixed q as a function of $\hbar$. This behavior is quite anomalous since one normally expects an exponential dependence in the tunneling tail.

Our semiclassical calculation qualitatively predicts this stretched exponential dependence well, as shown in Fig. 21. The reason for the quantitative discrepancy between the semiclassical and quantum calculations is the same as mentioned above. As the value of $\hbar$ increases, the KAM curve satisfying the resonance condition shifts outward. Correspondingly, the

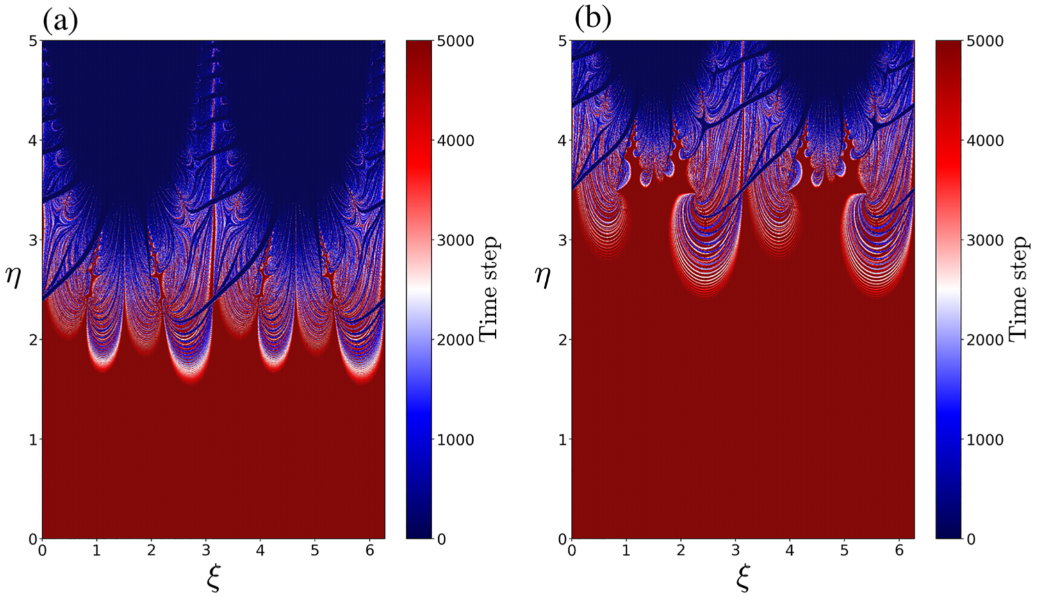

FIG. 22. The initial value plane (ξ, η), in which each color is assigned to reflect the number of time steps until the orbits leaving each point in the (ξ, η) plane leave a properly chosen finite-size box. The red regions show the set of initial points that remain in the finite region for a sufficiently long time, while the orbits in the blue region diverge to infinity within a short time. (a) $\lambda = 1.2$. (b) $\lambda = 3.0$. The parameters are set to $\tau = 0.01$, $\varepsilon = 1.0$.

complex orbits necessary to describe the transition should reach outer KAM curves, so the associated imaginary action becomes larger. However, we have to divide the imaginary action by $\hbar$ to calculate an individual semiclassical contribution of the form $\exp(-\text{Im}\, S_\gamma/\hbar)$. Thus, $\text{Im}\, S_\gamma$ increases with increase of $\hbar$, while the denominator is simply proportional to $\hbar$, so that a subtle balance arises from the competition between the denominator and the numerator in the imaginary phase $-\text{Im}\, S_\gamma/\hbar$. Our result shows that the resulting $\hbar$ dependence is stretched exponential, which is consistent with exact quantum calculations.

This stretched exponential dependence predicts a nontrivial nature in the complex classical dynamics. The above result shows that

$$\exp[-\text{Im}\, S(I_0, I)/\hbar] \sim \exp(-\hbar^{-\mu}), \tag{43}$$

where $\mu \sim 0.275$ is numerically estimated. Here I_0 and I denote initial and final actions, respectively. Assuming the classical quantization condition $I_0 = n_0\hbar$ and $I = n\hbar$ for the initial and final KAM curve, and also focusing on the decay of the height on a certain fixed plateau, meaning that $n - n_0$ is fixed, the above $\hbar$ dependence holds if

$$\text{Im}\, S(I_0, I) \sim (I - I_0)^{-(\mu-1)} \tag{44}$$

is satisfied. This is a relation that should hold in order to understand the observed phenomenon in the tunneling tail. This relation is purely classical, so it should be derived from the property of complex classical dynamics. This task is left for future investigation.

F. λ dependence of the step structure

As shown in Fig. 2, the step structure appears in the tunneling tail for a smaller λ case, while it is hidden in the tail of the ground-state contribution. The result given in Fig. 20 implies that this is due to the fact that the minimal imaginary action for the former case is smaller than that for the latter case. Since the smaller the value of η in the initial value plane (ξ, η), the smaller the imaginary action is, as discussed above, we can expect that the orbits with the minimal imaginary action for the smaller λ case will be found in a smaller η region in the (ξ, η) plane compared to the larger λ case.

The validity of such a prediction is almost confirmed by plotting the set K^+ in the (ξ, η) plane. The colors in Fig. 22 show the number of time steps until the orbits leaving each point in the (ξ, η) plane are out of a properly chosen finite sized box. Such a plot is expected to approximate the set K^+, as done in Fig. 9(a).

The boundary between the red and blue regions roughly indicates the natural boundary of the KAM curve supporting the ground states. Recall that our initial value curve Γ is determined to approximate such a supporting KAM curve. Since the orbits with the minimal imaginary action are close to the natural boundary, the comparison between Figs. 22(a) and 22(b) would lead to the prediction that the minimal imaginary action for the $\lambda = 1.2$ case is smaller than that for the $\lambda = 3.0$ case. This qualitatively explains the difference between Figs. 2(a) and 2(b).

VI. REAL ACTION OF COMPLEX PATHS AND QUANTUM RESONANCES

As shown in Fig. 4, the step structure shifts with the change of the Planck constant $\hbar$. This $\hbar$ dependence is explained by the fact that the step structure is caused by the quantum resonance. We can see the resonance in the plot of $|\langle\Psi_k^{(M)}|\Psi_0\rangle|^2$ [see Fig. 5(a)]. Small peaks found in the plot are responsible for creating the step structure in the plot of $|\langle q|\Psi_0\rangle|^2$ [see also

Fig. 5(b)]. Here we try to give a semiclassical understanding of this quantum resonance phenomenon.

Since the eigenfunction $|\langle\Psi_k^{(M)}|\Psi_0\rangle|^2$ is not directly accessible in the energy-domain semiclassical analysis, we consider the problem again from the time domain. Below we use the notation $|E\rangle$ instead of $|\Psi\rangle$ in order to represent the eigenstate of the integrable approximation.

For simplicity, we assume that the complex orbit with the minimal imaginary action is unique. In this case the semiclassical propagator can be expressed as

$$\begin{aligned}\langle E|\hat{U}^n|E_0\rangle &\simeq \sum_\gamma A_\gamma \exp\left[\frac{\mathrm{i}}{\hbar}S_\gamma(E,E_0)\right]\\ &= \sum_\gamma A_\gamma \exp\left\{\frac{\mathrm{i}}{\hbar}[S'_\gamma(E,E_0)+\mathrm{i}S''_\gamma(E,E_0)]\right\}\\ &\simeq A_{\gamma_{\min}} \exp\left[-\frac{1}{\hbar}S''_{\gamma_{\min}}(E,E_0)\right]\\ &\quad\times \exp\left\{\frac{\mathrm{i}}{\hbar}[S'_{\gamma_{\min}}(E,E_0)]\right\},\end{aligned} \tag{45}$$

where $S_\gamma(E,E_0)$ denotes the classical action of the orbit γ, which connects the initial state $|E_0\rangle$ and the final state $|E\rangle$, and A_γ the associated amplitude factor. The initial and final states are assumed to be the eigenstates of the Hamiltonian $H_{\mathrm{BCH}}^{(1)}$. $S'_\gamma(E,E_0)$ and $S''_\gamma(E,E_0)$ are the real and imaginary part of the action, respectively, and $\gamma_{\min}$ represents the complex orbit with the minimal imaginary action.

Let ω be the angular frequency of the KAM curve supporting the states $|E\rangle$. We can assume that the number of time steps during which the orbit travels along the associated KAM circle is N, where N is the period of oscillation of the quantum wave packet. Since $\tau \ll 1$ is assumed, we can approximate the discrete-time dynamics by the flow of the continuous Hamiltonian $H_{\mathrm{BCH}}^{(1)}$. Using the relation $\omega : \Omega = 1 : N$, the period T of one cycle for the flow system is given by $T = N\tau = 2\pi/\omega$. The classical action for one cycle

$$S(E) = \sum_{j=1}^{N}\{(q_j - q_{j-1})p_j - \tau[T(p_{j+1}) + V(q_j)]\} \tag{46}$$

admits the continuous approximation,

$$\begin{aligned}\widetilde{S}(E) &= \oint_E p\,dq - \int_0^{\frac{2\pi}{\omega}}[T(p)+V(q)]dt\\ &= 2\pi[I(E) - E/\omega]\\ &= \frac{2\pi N}{\Omega}[I(E)\omega - E].\end{aligned} \tag{47}$$

Here the action integral for one cycle

$$I(E) = \frac{1}{2\pi}\oint_E p\,dq \tag{48}$$

is introduced.

In the following, the number of iterations will be counted in units of one cycle over each KAM curve. Under such a count, the amount of action gained in a cycle is given by

$$S_{\mathrm{cycle}}(E) := \widetilde{S}(E)/N = \frac{2\pi}{\Omega}[I(E)\omega - E]. \tag{49}$$

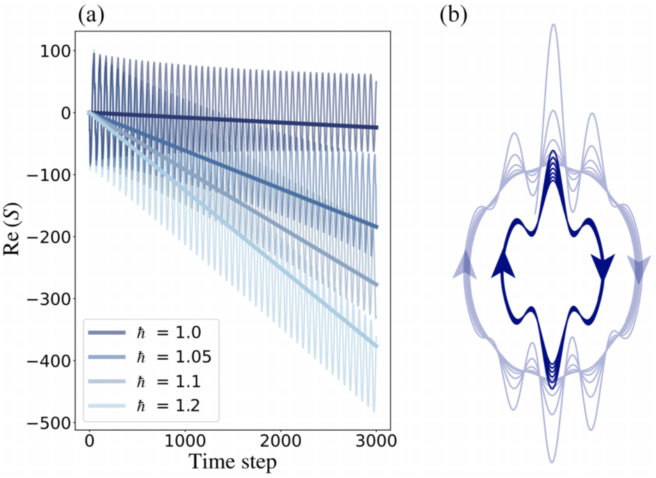

FIG. 23. (a) The behavior of the real action as a function of time step for different values of $\hbar$. (b) Schematic illustration showing the direction of rotation on different CRK curves.

As shown in Fig. 23, the real action increases while oscillating periodically in time, and we can confirm that the slope of the points taken at each period of oscillation follows the above formula (49).

Now suppose that the orbit, initially located on the manifold given by $H_{\mathrm{BCH}}^{(1)} = E_0$, rotates around it ℓ times. Then it moves to another manifold $H_{\mathrm{BCH}}^{(1)} = E$ and rotates around it also ℓ times. We can assume the existence of such an orbit due to the ergodicity of the dynamics in the complex plane. The action gained in the course of such itinerary should be

$$\begin{aligned}S'_{\gamma_{\min}}(E,E_0) &= \ell S_{\mathrm{cycle}}(E) - \ell S_{\mathrm{cycle}}(E_0)\\ &= \frac{2\pi\ell}{\Omega}\{[I(E)\omega - E)] - [I(E_0)\omega_0 - E_0]\}.\end{aligned} \tag{50}$$

Here we have neglected the real action contribution gained in the transition process from the initial manifold to the target manifold. This is justified by the fact that the orbit with the minimal action jumps almost instantaneously from the initial manifold to the final manifold. The minus sign in front of the second term is because the orbit rotates in the same direction on both manifolds [see the illustration in Fig. 23(b)].

We then recall the quantum resonance condition (12), which implies that

$$I(E)\omega - I(E_0)\omega_0 = m\hbar\Omega. \quad (m \in \mathbb{N}). \tag{51}$$

Here we assumed the Bohr-Sommerfeld quantization condition on each KAM curve.

Using the expression (50) together with (51), we find that

$$\begin{aligned}\lim_{n\to\infty}\langle E|\hat{U}^n|E_0\rangle &\simeq A_{\gamma_{\min}}\exp\left[-\frac{1}{\hbar}S''_{\gamma_{\min}}(E,E_0)\right]\\ &\quad\times\sum_{\ell=1}^{\infty}\exp\left[-\frac{\mathrm{i}}{\hbar}\frac{2\pi\ell}{\Omega}(E-E_0)\right].\end{aligned} \tag{52}$$

Since we are looking for the nature of the eigenfunction shown in Fig. 2, we include the iteration in the backward direction so that the sum should go from $\ell = -\infty$ to ∞. Applying the Poisson sum formula, we obtain that

$$\lim_{n\to\infty} \langle E|\hat{U}^n|E_0\rangle \simeq \hbar\Omega A_{\gamma_{\min}} \exp\left[-\frac{1}{\hbar} S''_{\gamma_{\min}}(E, E_0)\right] \times \sum_{n=-\infty}^{\infty} \delta(E - \hbar\Omega n). \tag{53}$$

The final expression is consistent with the observation made in Fig. 5(a). The mechanism that produces a series of peaks in the plot of $|\langle\Psi_n^{(M)}|\Psi_0\rangle|^2$ is explained by constructive interference of the complex orbit going back and forth between the initial and final manifolds.

Finally, we examine the validity of our assumptions. First, we have considered only a single orbit, while other complex orbits with imaginary actions comparable to the minimal imaginary action may come into play. This is very likely because the orbits are dense in the Julia set J. In every neighborhood of the orbit found to have the minimal imaginary action, there would be other complex orbits with almost the same imaginary action. If this is the case, we need to consider the initial phase differences between equally weighted orbits. There is no *a priori* information about such relative phases, but as shown in Fig. 10, it would be plausible to assume that there are correlations between orbits leaving different spots in the initial value plane (ξ, η). If the relative phases are completely random, the above scenario will not work because a sequence of δ functions in (53) will be killed by the random phase.

Another assumption is that we have only considered the repetition of the same number of rotations in both the initial and final manifolds. This may be somewhat artificial, but a core part of the argument is the constructive interference that occurs in both manifolds. Thus, we believe that the idea will essentially survive, even if explicit treatments become elaborate.

VII. CONCLUSION AND OUTLOOK

We have studied quantum tunneling of the ultra-near integrable system. The motivation for using the ultra-near integrable system is not to understand the nature of tunneling in such a special setting, but to elucidate general aspects of quantum tunneling in nonintegrable systems. So far, the study of dynamical tunneling has mostly been carried out in mixed systems, where the invariant structures inherent in nonintegrability, such as nonlinear resonances or chaotic seas, are relatively large. The phase space of such systems is, however, not well suited for dealing with exponentially small effects.

The most striking feature of the ultra-near integrable system studied in this paper and found in the previous paper [44] is that the tunneling tail exhibits the step structure, even though none of the visible structures, compared to the size of the Planck cell, arising from nonintegrability are present in classical phase space. In addition, the position and height of the steps move with the change of the Planck constant. The absence of visible nonintegrable structures implies that the so-called direct tunneling or instanton tunneling is not suitable for the explanation. The $\hbar$-dependent structures cannot be captured by the RAT theory either, because it assumes that classical nonlinear resonances in classical phase space mediate tunneling couplings. Obviously, individual nonlinear resonances are purely classical objects and do not move as a function of $\hbar$. Needless to say, CAT or chaotic tunneling cannot be applied because chaos does not spread widely in phase space.

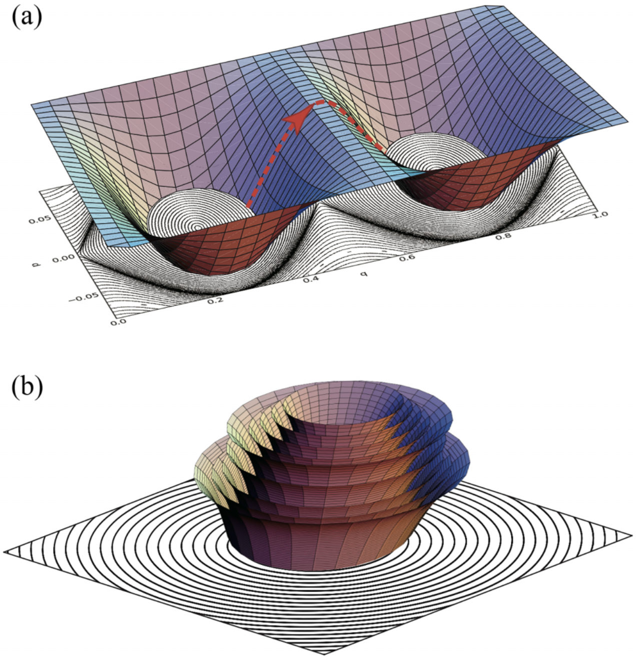

FIG. 24. Illustration of complexified invariant curves. (a) Double-well case with instanton path (red). (b) Single-well case without instanton path. In the latter case, the invariant curves are disconnected, so the transition between different invariant curves is strictly forbidden.

Our analysis based on the complex semiclassical method has revealed that the $\hbar$-dependent step structure can be understood as an interference phenomenon between the complex orbits with the minimal imaginary action. The stretched exponential scaling with respect to $\hbar$ can also be reproduced by the minimal imaginary action obtained by the procedure described in Sec. V. The stretched exponential scaling results from a subtly increasing rate of the imaginary action of the orbit associated with the state excited by the quantum resonance. These two nontrivial issues raised in [44] have thus been successfully resolved based on the fact that the underlying dynamics is ergodic in the complex plane. Since ergodicity is an inherent property of nonintegrable systems, we can conclude that the properties observed in tunneling tails are inherent to nonintegrable systems.

To illustrate the difference between tunneling in integrable systems and that in nonintegrable systems, imagine, for example, the phase space for the standard map, i.e., $V(q) = \sin q$ with $\tau \ll 1$ [see Fig. 24(a)]. In this case, the phase space profile is indistinguishable from the phase space of the one-dimensional pendulum Hamiltonian. For the pendulum Hamiltonian, the tunneling splitting occurs between the two quantum states whose classical supports have the same energy. The two states have different parities, and the exponentially small energy splittings are created between the associated states. Following the standard recipe, the width of the tunneling splittings can be evaluated semiclassically in terms of the instanton [13–15]. The same idea should work not only in one-dimensional but also in multidimensional systems as far as the system is completely integrable [59].

We can expect that the *instanton approximation* works if the system is close enough to the integrable limit. The classical phase spaces of completely integrable and slightly perturbed systems are almost identical, so such an expectation is plausible. Strictly speaking, as discussed in Sec. IV, complexified KAM curves cannot be analytic in the entire complex plane, so the instanton path breaks in the middle of the connection [69–72]. However, it is not surprising that there exists a range of the perturbation strengths in which the instanton approximation is still valid. In such a case, one may continue to use the instanton strategy even after it breaks. The basic idea adopted so far, including RAT theory, to analyze tunneling in nonintegrable systems is the integrable approximation of this kind.

However, the situation to which the instanton approximation can be applied is very limited. This is because the instanton path connects only the symmetrically located invariant curves [see Fig. 24(a)], which are reminiscent of separated equi-energy contours in the one-dimensional pendulum or double-well potential case. There are no paths connecting energy contours of different energies because equi-energy surfaces of different energies never intersect. There are no instanton path connections between neighboring invariant curves inside the separatrix [see Fig. 24(b)], or between an invariant curve inside the separatrix and the one outside the separatrix, and so on. There is no way to use the integrable approximation in such situations.

One might be tempted to think that the RAT scenario solves this problem, since it can assume successive tunneling transitions via nonlinear resonances lying between the initial and final states. Aside from the technical difficulties of finding appropriate sequences of nonlinear resonances, we encounter a fundamental limitation of the RAT scenario. One sticking point is, as pointed out above, is that the RAT scenario assumes nonlinear resonances comparable in size to the Planck cell. It cannot be applied to the situation where all nonlinear resonances are invisible on the scale of the Planck constant.

Even if we forget about the scale problem, nonlinear resonances alone cannot drive tunneling through the regular regime. This is because there are not enough nonlinear resonances to mediate all the invariant curves in the regular region. As shown in the KAM theorem, the invariant curves that survive after a perturbation occupy a positive measure in the angular frequency space. The surviving invariant curves have an irrational angular frequency, which satisfies the Diophantine condition. Since the Diophantine number has the positive measure in the irrational frequency space, the frequencies for which invariant curves survive are uncountably many, while the rational numbers are at most countably many. Nonlinear resonances arise from rational frequencies, so there are many invariant curves with irrational frequencies that cannot be mediated by nonlinear resonances. In addition to this fundamental difficulty, we must point out that the RAT scheme cannot deal with the transition across the separatrix [79], while anomalous enhancement of the tunneling probability is observed precisely when the tunneling transition across the separatrix comes into play [52].

Our claim in this paper is that the Julia set is an alternative to the instanton path, and the ergodicity in the Julia set ensures the tunneling coupling between arbitrarily separated regions in the real classical phase space. One can reach everywhere via the orbits in the Julia set, and the transition between arbitrarily disconnected regions in the real phase space becomes possible via the complex space. One may even say that quantum tunneling in nonintegrable systems is a manifestation of the ergodicity of classical dynamics in the complex plane.

Complex dynamical systems have been studied purely out of mathematical interest. As a result, physicists have been unaware of recent advances, especially in the topics discussed in this paper. However, for the reason explained here, the complex dynamical system would be an indispensable tool for understanding quantum tunneling in nonintegrable systems.

To proceed further, we need to have more precise control over the complex phase space. For this purpose, the ultra-near integrable setting could be an appropriate candidate to study in detail. The validity of the integrable approximation should be reexamined from this perspective. Although the orbits in the complex plane can come close to any point in the Julia set due to the ergodicity in the complex plane, the orbits moving close to the “reminiscent” of the instanton path must have some special property, otherwise the integrable approximation will not work. Answering this question would also reveal the role of classical nonlinear resonances.

Another point we would like to emphasize is that the step structure and the mechanism that produces it should not be taken to be limited to the ultra-near integrable setting. As shown in Sec. II, the step structure allows a clear interpretation based on the quantum resonance. The quantum resonance also leads to the step structure in the plot of the tunneling splittings ΔE as a function of $1/\hbar$ [52]. The plot of tunneling splitting or tunneling probability versus $1/\hbar$ is often used to observe the effect of classical nonlinear resonances on tunneling [7,48,52]. As discussed in [52,79], based on the Herring formula, one can show that the tunneling splitting can be well approximated by the value of the eigenfunction at an unstable fixed point located in the middle of the symmetric invariant curves. This means that the staircase structure in the plot of ΔE vs $1/\hbar$ implies the staircase structure in the plot of the value of the eigenfunction at a given point. As shown in the inset of Fig. 4, one can identify the staircase structure, although only a single step could be observed here due to the limitation of computational power. The step structure found in this paper and that observed in the plot of ΔE vs $1/\hbar$ are the opposite sides of the same coin.

As discussed in detail in [79], if the step structure and the resulting persistent enhancement are a crux characterizing tunneling in generic nonintegrable systems, it turns out that our task would be to elucidate the origin of the step structure in ultra-near integrable systems. Before studying the complex dynamics of nearly integrable systems with visible invariant structures, more detailed studies of ultra-near integrable systems should be highly desirable.

ACKNOWLEDGMENTS

The authors are grateful to Kensuke S. Ikeda, Yutaka Ishii, and Hidekazu Ito for stimulating discussions and helpful comments. This work has been supported by JSPS KAKENHI Grants No. JP17K05583 and No. JP22H01146.

---

[1] M. J. Davis and E. J. Heller, J. Chem. Phys. **75**, 246 (1981).
[2] S. C. Creagh, in *Tunneling in Complex Systems*, edited by S. Tomsovic (World Scientific, Singapore, 1998), p. 35.
[3] S. Keshavamurthy and P. Schlagheck, *Dynamical Tunneling: Theory and Experiment* (CRC Press, Boca Raton, 2011).
[4] O. Bohigas, S. Tomsovic, and D. Ullmo, Phys. Rep. **223**, 43 (1993).
[5] S. Tomsovic and D. Ullmo, Phys. Rev. E **50**, 145 (1994).
[6] O. Brodier, P. Schlagheck, and D. Ullmo, Phys. Rev. Lett. **87**, 064101 (2001).
[7] O. Brodier, P. Schlagheck, and D. Ullmo, Ann. Phys. **300**, 88 (2002).
[8] E. Doron and S. D. Frischat, Phys. Rev. Lett. **75**, 3661 (1995).
[9] A. Shudo and K. S. Ikeda, Phys. Rev. Lett. **74**, 682 (1995).
[10] A. Shudo and K. S. Ikeda, Physica D **115**, 234 (1998).
[11] S. C. Creagh and N. D. Whelan, Phys. Rev. Lett. **77**, 4975 (1996).
[12] S. C. Creagh and N. D. Whelan, Phys. Rev. Lett. **82**, 5237 (1999).
[13] B. Simon, Bull. Amer. Math. Soc. **8**, 323 (1983).
[14] B. Simon, Ann. Math. **120**, 89 (1984).
[15] S. Coleman, *Aspects of Symmetry: Selected Erice Lectures* (Cambridge University Press, Cambridge, 1988).
[16] C. G. Callan, Jr. and S. Coleman, Phys. Rev. D **16**, 1762 (1977).
[17] S. Coleman, Phys. Rev. D **15**, 2929 (1977).
[18] T. F. George and W. H. Miller, J. Chem. Phys. **56**, 5722 (1972).
[19] W. H. Miller, J. Chem. Phys. **61**, 1823 (1974).
[20] M. C. Gutzwiller, J. Math. Phys. **12**, 343 (1971).
[21] M. C. Gutzwiller, *Chaos in Classical and Quantum Mechanics* (Springer Science & Business Media, Berlin, 2013), Vol. 1.
[22] A. Shudo and K. S. Ikeda, *Dynamical Tunneling: Theory and Experiment* (CRC Press, Boca Raton, 2011), p. 139.
[23] R. Dingle, *Asymptotic Expansions: Their Derivation and Interpretation* (Academic Press, London, 1973).
[24] J. Écalle, *Les fonctions résurgentes: (en trois parties)*, vol. 1 (Université de Paris-Sud, Département de Mathématique, Bât. 425, 1981).
[25] A. Voros, Ann. l'I.H.P. Phys. Théor. **39**, 211 (1983).
[26] M. V. Berry, Publ. Math. Institut des Hautes Scientifiques **68**, 211 (1988).
[27] A. Shudo and K. S. Ikeda, Phys. Rev. Lett. **76**, 4151 (1996).
[28] A. Shudo and K. S. Ikeda, Nonlinearity **21**, 1831 (2008).
[29] A. Shudo and K. S. Ikeda, Nonlinearity **29**, 375 (2016).
[30] E. Bedford and J. Smillie, Invent. Math. **103**, 69 (1991).
[31] E. Bedford and J. Smillie, J. Amer. Math. Soc. **4**, 657 (1991).
[32] E. Bedford, M. Lyubich, and J. Smillie, Invent. Math. **114**, 77 (1992).
[33] E. Bedford and J. Smillie, Math. Ann. **294**, 395 (1992).
[34] S. Morosawa, Y. Nishimura, M. Taniguchi, and T. Ueda, *Holomorphic Dynamics*, Cambridge Studies in Advanced Mathematics (Cambridge University Press, Cambridge, 2000), Vol. 66.
[35] A. Shudo, Y. Ishii, and K. S. Ikeda, J. Phys. A **35**, L225 (2002).
[36] A. Shudo, Y. Ishii, and K. S. Ikeda, J. Phys. A **42**, 265101 (2009).
[37] A. Shudo, Y. Ishii, and K. S. Ikeda, J. Phys. A **42**, 265102 (2009).
[38] R. Koda and A. Shudo, J. Phys. A **55**, 174004 (2022).
[39] A. Shudo, Y. Ishii, and K. Ikeda, Europhys. Lett. **81**, 50003 (2008).
[40] S. D. Frischat and E. Doron, Phys. Rev. E **57**, 1421 (1998).
[41] A. Bäcker, R. Ketzmerick, S. Löck, M. Robnik, G. Vidmar, R. Höhmann, U. Kuhl, and H.-J. Stöckmann, Phys. Rev. Lett. **100**, 174103 (2008).
[42] A. Bäcker, R. Ketzmerick, and S. Löck, Phys. Rev. E **82**, 056208 (2010).
[43] A. Ishikawa, A. Tanaka, K. S. Ikeda, and A. Shudo, Phys. Rev. E **86**, 036208 (2012).
[44] R. Iijima, R. Koda, Y. Hanada, and A. Shudo, Phys. Rev. E **106**, 064205 (2022).
[45] O. Bohigas, D. Boosé, R. de Carvalho, and V. Marvulle, Nucl. Phys. A **560**, 197 (1993).
[46] G. M. Lando and A. M. O. de Almeida, Phys. Rev. Lett. **124**, 010402 (2020).
[47] P. Holoborodko, http://www.advanpix.com
[48] A. Bäcker, R. Ketzmerick, S. Löck, and L. Schilling, Phys. Rev. Lett. **100**, 104101 (2008).
[49] A. Shudo, Y. Hanada, T. Okushima, and K. S. Ikeda, Europhys. Lett. **108**, 50004 (2014).
[50] J. Le Deunff, A. Mouchet, and P. Schlagheck, Phys. Rev. E **88**, 042927 (2013).
[51] H. Harada, A. Mouchet, and A. Shudo, J. Phys. A **50**, 435204 (2017).
[52] Y. Hanada, A. Shudo, and K. S. Ikeda, Phys. Rev. E **91**, 042913 (2015).
[53] S. Löck, A. Bäcker, R. Ketzmerick, and P. Schlagheck, Phys. Rev. Lett. **104**, 114101 (2010).
[54] P. Schlagheck, A. Mouchet, and D. Ullmo, in *Dynamical Tunneling: Theory and Experiment*, edited by S. Keshavamurthy and P. Schlagheck (CRC Press, Boca Raton, 2011), p. 177.
[55] N. Mertig, J. Kullig, C. Löbner, A. Bäcker, and R. Ketzmerick, Phys. Rev. E **94**, 062220 (2016).
[56] F. Fritzsch, A. Bäcker, R. Ketzmerick, and N. Mertig, Phys. Rev. E **95**, 020202(R) (2017).
[57] K. Clauß, M. J. Körber, A. Bäcker, and R. Ketzmerick, Phys. Rev. Lett. **121**, 074101 (2018).
[58] J. H. Van Vleck, Proc. Natl. Acad. Sci. USA **14**, 178 (1928).
[59] S. C. Creagh, J. Phys. A **27**, 4969 (1994).

[60] V. G. Gelfreich, V. F. Lazutkin, C. Simó, and M. B. Tabanov, Int. J. Bifurcation Chaos **02**, 353 (1992).
[61] V. Lazutkin and C. Simó, Int. J. Bifurcation Chaos **07**, 253 (1997).
[62] S. Friedland and J. Milnor, Ergod. Theor. Dyn. Syst. **9**, 67 (1989).
[63] M. Hénon, in *The Theory of Chaotic Attractors*, edited by B. R. Hunt, T.-Y. Li, J. A. Kennedy, and H. E. Nusse (Springer, Berlin, 2004), pp. 94–102.
[64] R. Devaney and Z. Nitecki, Commun. Math. Phys. **67**, 137 (1979).
[65] H. Brolin, Ark. Mat. **6**, 103 (1965).
[66] M.-R. Herman, in *VIII-th International Congress on Mathematical Physics (Marseille)*, edited by M. Mebkhout and R. Sénéor (World Scientific, Singapore, 1986), pp. 138–184.
[67] J.-C. Yoccoz, Astérisque **231**, 3 (1996).
[68] C. L. Siegel, Ann. Math. **43**, 607 (1942).
[69] I. C. Percival, Physica D **6**, 67 (1982).
[70] J. M. Greene and I. C. Percival, Physica D **3**, 530 (1981).
[71] A. Berretti and L. Chierchia, Nonlinearity **3**, 39 (1990).
[72] A. Berretti and S. Marmi, Phys. Rev. Lett. **68**, 1443 (1992).
[73] R. Krikorian, Publ.math.IHES **135**, 1 (2022).
[74] R. L. Devaney, *An Introduction to Chaotic Dynamical Systems* (CRC Press, Boca Raton, 2021).
[75] E. Delabaere, H. Dillinger, and F. Pham, J. Math. Phys. **38**, 6126 (1997).
[76] T. Kawai and Y. Takei, *Algebraic Analysis of Singular Perturbation Theory*, Iwanami Series in Modern Mathematics, Vol. 227 (American Mathematical Society, Providence, RI, 2005).
[77] M. V. Berry and C. J. Howls, Proc. R. Soc. London **434**, 657 (1991).
[78] C. Howls, Proc. R. Soc. London A **453**, 2271 (1997).
[79] Y. Hanada, K. S. Ikeda, and A. Shudo (unpublished).